Eikonal tomography of the Southern California plate boundary region

H. Qiu[1], F.C. Lin[2], and Y. Ben-Zion[1]

[1]Department of Earth Sciences, University of Southern California, Los Angeles, CA, USA

[2]Department of Geology and Geophysics, The University of Utah, Salt Lake City, UT, USA

Corresponding author: Hongrui Qiu (hongruiq@usc.edu)

Key Points:

- Reliable surface wave phase and group dispersion curves for 2.5-16 s are extracted from ambient noise cross-correlations
- Eikonal tomography yields robust isotropic phase and group velocities using an irregular seismic network in southern California
- Joint inversion of phase and group velocities significantly improves the velocity structure in the top 3-20 km, particularly near faults

Abstract

We use Eikonal tomography to derive phase and group velocities of surface waves for the plate boundary region in southern California. Seismic noise data in the period range 2 and 20 s recorded in year 2014 by 346 stations with ~1-30 km station spacing are analyzed. Rayleigh and Love wave phase travel times are measured using vertical-vertical and transverse-transverse noise cross-correlations, and group travel times are derived from the phase measurements. Using the Eikonal equation for each location and period, isotropic phase and group velocities and 2-psi azimuthal anisotropy are determined statistically with measurements from different virtual sources. Starting with the SCEC Community Velocity Model, the observed 2.5-16 s isotropic phase and group dispersion curves are jointly inverted on a 0.05°×0.05° grid to obtain local 1D piecewise shear wave velocity (Vs) models. Compared to the starting model, the final results have generally lower Vs in the shallow crust (top 3-10 km), particularly in areas such as basins and fault zones. The results also show clear velocity contrasts across the San Andreas, San Jacinto, Elsinore and Garlock faults, and suggest that the San Andreas fault southeast of San Gorgonio Pass is dipping to the northeast. Investigation of the non-uniqueness of the 1D Vs inversion suggests that imaging the top 3 km Vs structure require either shorter period (≤ 2s) surface wave dispersion measurements or other types of dataset such as Rayleigh wave ellipticity.

1. Introduction

The boundary between the North American and Pacific plates in Southern California (SC) has several major faults, including the San Andreas Fault (SAF), San Jacinto Fault (SJF), Garlock Fault (GF), and Elsinore Fault (EF). These and other faults separate the SC crust into several distinctive geologic provinces including the Southern Central Valley, Sierra Nevada and Mojave Desert in the north; the Western, South-Central and Eastern Transverse Ranges plus Eastern California Shear Zone (ECSZ) in the center; and the Ventura Basin, Los Angeles (LA) Basin, Peninsular Ranges, and Salton Trough in the south (Fig. 1). Having a good 3D tomographic model is crucial for understanding structural properties such as continuity and dipping of the major faults, and providing an accurate framework for inversions of earthquake source properties, calculations of seismic ground motion and other topics.

Several local and regional tomographic models of SC with a variety of spatial scales (0.5 km to the entire SC) and resolutions (tens of meters to >5 km) have been developed in previous studies. Methods using fault zone phases (e.g. Qiu et al., 2017; Share et al., 2017; Qin et al., 2018), body wave travel times (e.g. Allam et al., 2012, 2014; Share et al., 2019), surface wave tomography based on earthquakes (e.g. Alvizuri & Tanimoto, 2011; Prindle & Tanimoto, 2006; Yang & Forsyth, 2006) and ambient noise (e.g. Zigone et al., 2015; Barak et al., 2015; Berg et al., 2018), joint inversion of body and surface waves (e.g. Fang et al., 2016), and full inversion of waveforms with periods ≥ 2-5s (e.g. Tape et al., 2010; Lee et al., 2014) have been applied in this region. Each of these models resolves different components of the crustal structures due to variations in data sensitivity and quality (e.g. uncertainty), non-uniqueness and parameterization of the inversion process (e.g. regularization and smoothing). A combination of tomographic models that incorporates different types of data and seismic network configurations provides a clear illustration of the structural complexity in the SC region (e.g., Shaw et al., 2015).

Noise based surface wave tomography has been shown to be effective in resolving 3D Vs crustal structure either for the entire SC region (e.g. Barak et al., 2015) or more focused local areas (e.g. Zigone et al., 2015; Fang et al., 2016). Although the noise sources are not isotropically distributed in the SC plate boundary region, the biases in surface wave dispersions measured from ambient noise cross-correlations (ANC) have been shown to be minor (e.g. Hillers et al., 2013). Surface waves are typically assumed to propagate on the great circle path connecting the virtual source and receiver, and the corresponding velocity structures are resolved using all available source-receiver pairs (Barmin et al., 2001).

In contrast to the conventional surface wave tomography method, Eikonal tomography accounts for ray bending and determines phase velocities by solving the Eikonal equation across phase travel time maps (Lin et al., 2009). Through statistical analysis of velocity measurements obtained from different sources, isotropic phase speeds together with azimuthal anisotropy and corresponding uncertainty estimates can be determined. Eikonal tomography method was first applied across the USArray (Lin et al., 2009), and the derived isotropic phase results were shown to be slightly slower, on average, compared to those from straight-ray tomography, particularly in SC. The differences suggest that it is necessary to take the ray bending effect into consideration in order to obtain better phase velocity estimates.

In the present paper, we use the ANC computed from stations of the regional SC seismic network and apply Eikonal tomography to resolve phase and group velocity maps. The results have finer grid size (i.e. 0.05°×0.05°), broader period range toward short periods (i.e. 2.5s-16s), and better data coverage compared to previous studies (e.g. Lin et al., 2009; Roux & Ben-Zion, 2017). In section 2, we describe the data used in the study and the necessary processing steps to calculate reliable ANC for each station pair. Considering the vast number of station pairs, we adopt the modified automatic Frequency Time Analysis (FTA) developed by Bensen et al. (2007) and Lin et al. (2008) to obtain both phase and group dispersion measurements. Following the flow chart shown in Figure 2, we describe the procedures to measure the surface wave travel times as a function of period for every station pair in section 3.

In section 4.1, we review the methodology of Eikonal tomography and its underlying assumptions. Different from previous Eikonal tomography studies (e.g. Lin et al., 2009, 2013; Ritzwoller et al., 2011; Gouédard et al., 2012; Xu et al., 2016) that use evenly spacing seismic arrays, the station spacing for the SC seismic network is rather irregular, with ~1-5 km near SJF and SAF, ~5 km in LA and Ventura basins, and ~10-30 km in Mojave desert and ECSZ (Fig. 1). We thus also discuss the inclusion of several additional quality control criteria to ensure the reliability of the resulting phase velocities. Furthermore, we derive group velocities from a modified Eikonal tomography procedure, which is also discussed in section 4.1. The resulting isotropic phase and group speeds (section 4.2) are used to infer a new Vs model for the SC plate boundary region.

The Vs inversion is first performed at each grid cell and then assembled together to construct the final 3-D Vs model in section 5. The final surface wave phase speed and Vs models are compared to tomographic models obtained from previous studies, and the prominent geological structures that observed in our models are discussed in section 5.2. The technical improvements and updated geophysical knowledge achieved in our final models are summarized in Section 6. In addition to resolving better some crustal components, the results complement the existing knowledge on large-scale fault structures (velocity contrasts, fault dipping) in the SC plate boundary region.

2. Data

We download all available continuous waveforms recorded by 346 stations (with 299 being three-component; Fig. 1) in the SC plate boundary region during the entire year of 2014. Seismic stations from several SC seismic networks, including the Anza network (AZ; Vernon, 1982), the California Integrated Seismic network (CISN), the San Jacinto Experiment network (YN; Vernon & Ben-Zion, 2010), the Plate Boundary Observatory Borehole network (PB), the Southern California Seismic network (CI; SCEDC, 2013), and the UC Santa Barbara Engineering Seismology Network (SB) are used. This combined seismic network includes 238 broadband and 108 short-period sensors, covering the ~600 km aperture study region with typical station spacing varying from 1 km to 30 km.

Noise preprocessing steps are essential to increase the quality and accuracy of surface wave signals extracted from the noise cross-correlation method (e.g. Shapiro & Campillo 2004; Bensen et al., 2007; Poli et al., 2012; Boue et al., 2013; Zigone et al., 2015). In this study, we follow closely to the method described by Zigone et al. (2015) to compute daily ANC between all available station pairs and components. The computed multi-component ANC are then rotated to the coordinate system of vertical (Z), radial (R), and transverse (T) directions by viewing one station as the source and the other as the receiver (Lin et al., 2008). Figs. 3a&b shows the resulting daily ANC for ZZ component at two example station pairs – the coast parallel pair DJJ-GOR and the coast perpendicular pair GSC-SDD. For both station pairs, coherent surface wave arrivals are observed on both positive and negative correlation time lags in the daily cross-correlograms throughout the year. These daily correlation functions are stacked over the entire year to further enhance the signal to noise ratio (SNR; Figs. 3c&d). In this paper, we use the stacked ZZ and TT component ANC to measure the Rayleigh and Love wave travel time dispersions, respectively. Since higher mode surface waves (e.g. blue star in Fig. 4) are only observed in ANC at high frequencies (e.g. 2-5s) for specific station pairs (e.g. across basins), all subsequent results and discussions refer to the fundamental mode surface waves.

In SC, ambient noise seismic waves are mostly excited from oceanic waves in the southwestern direction (e.g. Kedar & Webb, 2005; Hillers et al., 2013), which results in the asymmetry of ANC particularly for coastline normal station pairs (e.g. Figs. 3b&d). Despite the apparent noise directionality, earlier studies suggest that surface wave dispersion can still be reliability extracted from ANC in this area (e.g. Shapiro et al., 2005; Hillers et al., 2013). To further enhance the signal and effectively homogenize the noise wavefield, we calculate the "symmetric signal" by folding and averaging the waveforms on both the positive and negative time lags (e.g. Lin et al., 2007). In general, the symmetric signal often has a higher SNR (due to the suppression of incoherent noises within the two time lags) and allows the dispersion curve to be determined across a broader period range. We note that the Eikonal tomography approach used in this study determines local surface phase velocities based on relative travel time measurement and is also less sensitive to inhomogeneous noise source distribution as discussed in Lin et al. (2013).

3. Automated dispersion picking

Figure 4 shows the one-year stacked ZZ component ANC and the symmetric narrow bandpass filtered signals for the example coastline normal station pair GSC-SDD. Clear period dependent travel time and SNR can be observed. Considering the vast number of ANC (~ 40,000 for ZZ component and ~ 30,000 for TT component), we adopt a modified automated dispersion picking algorithm of Bensen et al. (2007) to extract surface wave travel times for periods between 2s and 20s. The procedures are described in detail below.

3.1 Frequency Time Analysis (FTA)

Figure 5 illustrates the standard procedures of FTA applied on the example station pair GSC-SDD. First, we taper the time series using a window (dashed lines in Fig. 5a) that outlines the surface wave signal (i.e. between the assumed 4.0 km/s and 1.5 km/s maximum and minimum velocities) and define the waveforms in the window with an assumed velocity lower than 1.5 km/s as the noise. Then, a series of Gaussian narrow bandpass filters centered on different angular frequencies, ω_k , $G(\omega,\omega_k)=\exp\left\{-\alpha\left[\left(\omega-\omega_k\right)/\omega_k\right]^2\right\}$, are applied to the tapered waveform. Here α is a unitless parameter that controls the width of the Gaussian filter, which we set to 20 based on trial and error. Then the amplitude and phase components of the filtered signal, $S^f\left(t,\omega_k\right)$, can be written as:

$$S^f\left(t,\omega_k\right)=\left|A\left(t,\omega_k\right)\right|\cdot e^{i\varphi\left(t,\omega_k\right)}, \tag{1}$$

where $\left|A\left(t,\omega_k\right)\right|$, $\varphi\left(t,\omega_k\right)$ are the corresponding envelope and phase functions in the time domain, and t is the lapse time. The envelope and phase functions at 7s are illustrated in Fig. 5b. Figure 5c shows a 2-D amplitude diagram that aligns the envelope functions with respect to the corresponding central periods $T_k=2\pi/\omega_k$. This 2-D amplitude diagram is later used to determine travel time dispersion in section 3.2

For different station pairs, the period range in which we can extract good quality surface wave signals can vary significantly. To determine the proper period range for FTA, we first set a maximum cut-off period as $T_{\max} = \Delta/(2c) \approx \Delta/6$ to satisfy the far field approximation (Bensen et al., 2007). Here Δ is the interstation distance in kilometers, and c is the assumed reference phase velocity and is set to be 3 km/s (Fig. S1). In the case of $T_{\max} > 20$s, we set $T_{\max} = 20$s. Then, we calculate the preliminary period dependent SNR as the ratio between the maximum amplitude of the envelope function and the root mean square amplitude within the noise window. For each ANC, we only perform FTA for the period range in which the SNR is larger than 5.

3.2 Determination of phase traveltime dispersions

The surface wave phase travel time dispersion can be obtained from the phase function $\varphi\left(t,\omega_k\right)$ using equation derived in Lin et al. (2008) by assuming the source phase ambiguity term λ equal to 0:

$$t_{ph}\left(\omega\right)=\left[\varphi\left(t,\omega_k\right)+\omega t-\frac{\pi}{4}-N\cdot 2\pi\right]\Big/\omega. \tag{2}$$

Here, N is the cycle skipping ambiguity term, which can be resolved using a reference dispersion relation. Note that the instantaneous angular frequency $\omega = \partial\varphi\left(t,\omega_k\right)/\partial t$ can be slightly different from the central angular frequency ω_k of the applied filter. To resolve cycle skipping ambiguity, N, we take advantage of the existing high-resolution Community Velocity Models for SC (i.e. Shaw et al., 2015 – CVM-H15.1; Lee et al., 2014 – CVM-S4.26). First, we compute synthetic phase travel time dispersion for each station pair based on the model CVM-S4.26. At each grid point, we extract the 1-D P- and S-wave velocity depth profiles and calculate the corresponding phase velocity dispersion curves (Herrmann, 2013). By compiling these phase velocity dispersion curves at all locations, we construct a series of 2-D phase velocity maps at different periods. For each period, we calculate the synthetic surface wave phase travel time for every station pair based on the 2-D phase velocity map using the fast marching method (Sethian, 1996). The model predicted pairwise phase travel time dispersion curve is then used as a reference to constrain the travel times measured through the ANC.

Ideally, phase travel time can be measured at any selection of lapse time t within the surface wave window following equation 2. But, in practice, phase travel time is often evaluated at the time of the envelope peak, $t = t_g\left(\omega\right)$, to guarantee a maximum SNR (e.g. Aki & Richards, 2002; Lin et al., 2008). Figure 4 shows the envelope functions and corresponding $t_g\left(\omega\right)$ for various periods (red star), and we find the global maximum at 2s period is abnormally fast (i.e. faster than the signals observed at longer periods). This indicates that either the noise source distribution is not sufficiently homogeneous or the signal is dominated by strong body waves or higher mode surface waves (e.g. Boúe et al., 2016; Ma et al., 2016; Savage et al., 2013) at this period. In this case, instead of evaluating the phase travel time at the global peak, the lapse time of another local maximum should be used (i.e. the blue star in Fig. 4). Considering the vast number of station pairs used in this study, we develop an automatic procedure to filter out these abnormal envelope peaks. First, we set a “reasonable travel time range” for each station pair and rule out envelope peaks (both local and global ones) that are outside the range as well as those peaks with SNR less than 5. Considering the envelope should propagate slower than the phase, we use the phase travel time predicted from the reference CVM-S4.26 model (red dashed lines in

Fig. 4 and Fig. 5c) to determine the lower bound for group travel time $t_g(\omega)$. In addition, considering the CVM-S4.26 model is derived using data with frequencies lower than 0.2 Hz (Lee et al., 2014) and it may yield poor predictions at short periods, we further reduce the lower bound based on a linearly varying scale of 5% and 0% between 2s and 20s period (black dashed curve in Figure 5c).

After filtering out erroneous envelope peaks, we further require the candidate $t_g(\omega)$ (e.g. red stars in Fig. 5c) to be continuous as a function of periods. To ensure the continuity, we use the second order derivative edge detection algorithm to find possible jumps in the $t_g(\omega)$ dispersion curve, and fix the discontinuity, if detected, following the procedure of Bensen et al. (2007).

3.3 Determination of group traveltime dispersions

Theoretically, the surface wave group travel time is given by the lapse time, $t_g(\omega)$, where the envelope function $|A(t,\omega_k)|$ reaches the maximum amplitude (Aki & Richards, 2002). In Figure 5, we use the surface wave from the symmetric signal of the one-year stacked ANC to demonstrate the picking process (Fig. S2 for results using causal and acausal sides). Figure 6 shows the resulting Rayleigh wave phase travel time along with the continuous $t_g(\omega)$ dispersion curves measured at the casual side, acausal side, and the symmetric signal of the correlation function for station pair GSC-SDD. While consistent phase travel time dispersion curves are obtained from all three cases, significant discrepancies are observed between the $t_g(\omega)$ dispersion curves, especially at longer periods (> 15s), suggesting that the peak of envelope function is sensitive to noise and often associated with large uncertainties (Fig. 6d and Fig. 7a). Therefore, in this study, instead of determining group travel time based on $t_g(\omega)$ (e.g. Barak et al., 2015; Zigone et al., 2015), we simply derive the group travel time from the smoothed phase dispersion using the following relation:

$$\upsilon_{gp} = \upsilon_{ph} - \lambda \cdot \partial \upsilon_{ph} / \partial \lambda . \quad (3)$$

where υ_{ph} and υ_{gp} represent the smoothed phase and resulting group dispersions in the form of average velocities (i.e. $\upsilon_{ph} = \Delta / t_{ph}$, $\upsilon_{gp} = \Delta / t_{gp}$) and λ is the wavelength given by $2\pi \cdot \upsilon_{ph} / \omega$. Here, we use the observed phase dispersion to first invert for a 1D Vs model and then predict the smoothed phase velocity dispersion to stabilize the first derivative in equation 3 (Fig. 7).

Although the phase derived group travel times do not provide additional independent constraints to the earth structure, using both phase and group dispersion curves stabilizes the 1-D Vs inversion and yields better results of Vs structure than those using phase dispersions alone. This is mostly due to the differences in depth sensitivity kernels of the group and phase velocities (Fig. S3) that helps reducing non-uniqueness inherent in the inversion (Moschetti et al., 2010; Li et al., 2012; Herrmann, 2013).

3.4 Quality control

As Eikonal tomography determines velocities based on first order spatial derivative of travel time maps, the result is very sensitive to erroneous travel time measurements (e.g. Lin et al., 2009). Because of that, it is crucial to identify and remove as much erroneous travel time measurements as possible. In this section, we introduce the following three selection criteria to control the quality of the travel times measured following procedures in section 3.2 and 3.3:

(1) Consistency between symmetric, causal, and acausal signals. Here we reject dispersion measurements with inconsistent phase dispersion between causal, a-causal, and the symmetric component signals. Here we calculate the phase travel time differences between measurements of the symmetric and causal components at each period, and select the period range that yields discrepancies less than 5%. Such period range can also be obtained by comparing phase dispersions of the symmetric and acausal signals. The phase dispersion curves within the union of these two period ranges are considered to be robust. A complete description of the determination of consistency between phase travel time dispersion curves can be found in the supplementary material (Appendix I).

(2) Consistency with the reference model. As no major discrepancy is expected between the observed and reference predicted dispersion curves in particularly at the long periods, two additional selection criteria are introduced for phase dispersion measurements. First, the predicted and observed travel time difference at the longest measurable period (T_1) should be smaller than $0.3T_1$. Second, the average predicted and observed travel time difference in the top one-third of the measurable period range should be smaller than 0.4 of the average period in that range. Dispersion curves that do not satisfy the above criteria are discarded.

(3) Minimum period range requirement. Since the predicted reference dispersion curve is only considered reliable at periods larger than 5s (Lee et al., 2014), we reject all dispersion curves with either the longest measurable period T_1 smaller than 6s or the measurable period range shorter than 2.5s.

Figure 8 shows the histograms of the phase and group travel times that pass the above quality selection criteria for 3s, 7s, and 11s Rayleigh and Love waves. Since there are fewer three-component stations in the seismic network and the SNR of Love waves is generally smaller than that of Rayleigh waves, the total number of travel time measurements is significantly higher (i.e. ~40%-50% more) for Rayleigh waves. Based on the distributions of the measurements, we find that the width of the histogram (i.e. standard deviation) decreases as period increases, and the histograms of Love waves are wider than those of Rayleigh waves. These observations are likely due to higher degree of lateral heterogeneity at shallower depth and the broader spatial sensitivity of longer period waves. Since SNR is lower at shorter periods, the poor quality of short period dispersion measurements also contributes to the large width of the corresponding histogram. The median average speed (i.e. peak of the histogram) increases with period, which is consistent with the fact that shear wave velocity generally increases with depth, and is faster for Love waves.

4. Eikonal tomography

4.1 Methodology

Different from the traditional straight-ray tomography (e.g. Barmin et al., 2001), Eikonal tomography accounts for ray bending in the surface wave propagation and is based on the

Eikonal equation

$$\vec{s}_{ij} = \vec{e}_{ij} / \upsilon_{ij} = \nabla \tau_i \left(\vec{x}_j \right), \tag{4a}$$

which is derived from the 2-D Helmholtz wave equation (e.g. Wielandt, 1993; Lin & Ritzwoller, 2011) by neglecting the term associated with the amplitude Laplacian:

$$\frac{1}{\upsilon_{ij}^2} = \left| \nabla \tau_i \left(\vec{x}_j \right) \right|^2 - \frac{\Delta A_i \left(\vec{x}_j \right)}{A_i \left(\vec{x}_j \right) \omega^2}, \tag{4b}$$

where i and j indicate the virtual source and grid point indexes, $\vec{s}$ and $\vec{e}$ are local slowness and the unit vectors orienting towards the wave propagation direction, τ_i is the phase travel time, $\vec{x}_j$ is location of the j-th grid cell, A is the wave amplitude, and ω is the angular frequency. In Eikonal tomography, phase velocity structure can be simply inferred locally by applying the inverse operator – the spatial gradient to the phase traveltime field without constructing the forward operator. It is straightforward and computational less intensive compared to the straight-ray tomography. Lin and Ritzwoller (2011) refers the phase velocity derived from Eikonal equation as the "apparent" phase velocity and that calculated via Helmholtz equation as "corrected" phase velocity. These two velocities are approximately equal when 1) the angular frequency, ω, is sufficiently high or 2) the amplitude field is smooth enough so that the amplitude Laplacian is negligible. Although the group travel time does not obey the Eikonal equation 4a, based on the assumption that the propagation of the surface wave envelope is the same as indicated by the phase front, we can apply a modified version of Eikonal equation:

$$\vec{s}_{ij}^{g} = \vec{e}_{ij} / \upsilon_{ij}^{g} = \nabla \tau_i^{g} \left(\vec{x}_j \right), \tag{5}$$

to infer the local group velocity, where $\vec{s}_{ij}^{g}$, υ_{ij}^{g}, and τ_i^{g} represent the local group slowness vector, group speed, and group travel time field, respectively.

Following the procedure developed in Lin et al. (2009), for each common station, all available phase or group travel times associated with the central station (Fig. S4a) are used to construct a travel time map on a 0.05°×0.05° grid (Fig. S4b). The minimum curvature interpolation method (Smith & Wessel, 1990) is used. Despite all the quality selection criteria we developed in section 3.4, to obtain smooth travel time map, we impose additional quality control criteria to remove outlier travel times that are not consistent with their nearby measurements. Specifically, we reject any travel time measurement that meets any of the two following conditions: 1. The amplitude of travel time gradient at the station location is less than 0.25 s/km or larger than 2 s/km (green circles in Fig. S4c). 2. While the first criterion is capable of identifying most of the low quality data, trial and error indicates that the resulting speed maps are more stable by further removing measurements that produce large curvature values. The curvature of travel time field at the station location is identified as an outlier when larger than 2 times the standard deviation computed over the entire map (≥ 0.07s/km for 2.5s and ≥ 0.04s/km for 16s; red circles in Fig. S4c). This step is necessary as the station spacing is highly irregular and the second order derivative is more effective in detecting outliers when data coverage is sparse. After removing the outliers, new travel time maps are then regenerated and phase propagation direction and local phase and group slowness can be evaluated through equation 4a (Fig. S4d) and equation 5 at each grid point.

Unlike the Eikonal tomography performed on USArray by Lin et al. (2009), the southern California seismic network used in this study is highly irregular (Fig. 1) with regions that have various distinctive station spacing configurations: ~1-5 km near the major faults, and ~5 km within basin areas, and ~10-30 km for other regions (e.g. ECSZ). Because of this uneven station distribution, it is essential to identify regions with robust and reliable travel time interpolation, and only estimate the travel time gradient within these areas. We first adopt the criteria used in Lin et al. (2009), including truncation of regions that are within two wavelengths of the virtual source location, "three- out of four-quadrant selection criterion" with a searching radius of 50 km, and comparison of phase travel time interpolation with two different surface tension (Figs. S5a&b).

In order to further tackle the irregular array configuration, we introduce the concept of "station configuration error" and further remove regions that are highlighted by large error values. Similar to the idea of a synthetic checkerboard test (Lévěque & Wittlinger, 1993), which provides an estimation of the spatial resolvability for specific data coverage, we perform synthetic tests to evaluate the station configuration error for Eikonal tomography. First, for each virtual source, we compute the synthetic travel times for the same station configuration assuming a homogeneous phase speed υ_{syn}. Then we apply Eikonal tomography to the synthetic travel times and obtain an estimated 2-D phase speed map with υ_i^{inv} representing the local phase speed at the *i*-th grid cell. The station configuration error δ_i at the *i*-th grid point is defined as

$$\delta_i = \left|\upsilon_{syn} - \upsilon_i^{inv}\right| / \upsilon_{syn} . \tag{6}$$

Here we use a threshold of 0.025 to further truncate regions with poor station coverage (Fig. S6c).

Figure 9 shows the resulting phase velocity maps for 7s Rayleigh waves using 4 different stations as the virtual source. Colors and arrows represent the estimated local phase speed and propagation direction, respectively. Patterns that match well with the surface geological feature, such as low velocity zones in LA basin, Salton Trough, and near faults, are consistently observed in all the maps. However, there are also differences found between these maps. Part of these differences can be explained by azimuthal anisotropy. In general, the phase velocity map based on individual effective source (Fig. 9) is noisy due to erroneous phase travel times that we are unable to remove completely using the quality selection criteria. However, previous Eikonal tomography studies (e.g. Lin et al., 2009, 2013) showed that these errors could be significantly suppressed through stacking. The resolution of the resulting speed maps is controlled by the grid size and local station spacing (e.g. Fig. 12 of Lin et al., 2009), suggesting a spatial resolution of 5-15 km in the center areas with dense station coverage and 15-30 km in regions on the edge.

Since a non-negligible azimuthal anisotropy effect is observed in this region (Fig. S6), to avoid biases in the stacking process, for each location, we first weight each slowness measurement s_i inversely proportional to the number (n_i) of measurements that has an azimuth different from the target measurement by less than 20°:

$$s_i' = \frac{1}{n_i} s_i . \tag{7}$$

Let normalization coefficients $\eta = \sum_{i=1}^{N} \frac{1}{n_i}$ and $\xi = \sum_{i=1}^{N} \frac{1}{n_i^2}$, then the weighted mean slowness, s_0, and the corresponding standard deviation, σ_{s_0}, are given by:

$$s_0 = \frac{1}{\eta} \sum_{i=1}^{N} s_i', \tag{8a}$$

$$\sigma_{s_0}^2 = \frac{\xi}{\eta^3 - \eta \cdot \xi} \cdot \sum_{i=1}^{N} \frac{1}{n_i} \left(s_i - s_0\right)^2, \tag{8b}$$

where N is the total number of slowness measurements available at the location from different virtual sources.

4.2 Isotropic phase and group speed maps

Figures 10 and 11 show the resulting stacked isotropic phase and group speed maps for 3s, 7s, and 11s Rayleigh waves with corresponding uncertainty distributions. The isotropic speed maps for Love waves are shown in Figs. S7&S8. Azimuthal anisotropy can also be derived for each location at different periods (e.g. Fig. S6), but in this paper, we only focus on the isotropic phase and group velocities. The anisotropy results will be discussed in a separated study.

The isotropic phase and group speed maps at 3s (top left of Fig. 10, 11, S7, and S8) agree well with the surface geology. Low velocity zones (LVZ) are observed at Southern Central Valley, basins (e.g. LA basin, Ventura basin, San Bernardino basin), Salton Trough, and complex fault junctions (e.g. SGP, the Trifurcation area in SJFZ). Higher velocities (~3 km/s) are seen in regions such as the Peninsular Ranges. The LVZ below the basins and Salton Trough show a flower-type structure (e.g. Zigone et al., 2015), width decreases with depth or period. Clear velocity contrasts are found across surface traces of the major faults (e.g. SJF, SAF). The Peninsular Ranges have the fastest velocity values of the entire map for all periods. Consistent with the increasing histogram peak velocity with period shown in Fig. 8, faster velocities are observed for the isotropic phase and group maps at longer periods. The obtained Rayleigh wave phase and group speed maps are generally similar to results from previous studies (Barak et al., 2015; Zigone et al., 2015; Roux & Ben-Zion, 2017) in the overlapping area, with our phase and group velocities being slightly slower beneath basins (e.g. LA basin and Ventura basin) and showing sharper velocity contrast across the SAF southeast to the SGP at shorter periods (< 7s).

The uncertainties, calculated using equation 8b, provide an estimate of the variability in velocities derived from different virtual sources. Larger uncertainties are observed at shorter periods. This may indicate the quality of isotropic speed maps is lower or the azimuthal anisotropy (e.g. Fig. S6) is larger at the shorter period compared to those at the longer period. In addition, while the spatial distribution of uncertainties is similar, larger values are also observed for the group speed than the phase speed, as phase dispersion is intrinsically smoother and more stable than group dispersion (eq. 3). In addition, we find larger uncertainty values at the edge of the model (e.g. south of Salton Trough, Southern Central Valley), and this is due to a poor azimuthal and station coverage. The uncertainty distributions for Love waves (Fig. S7&S8) show a similar pattern but with generally larger values, as both the data quality is poorer and the depth sensitivity is larger at shallower depths (Fig. S3) for Love waves than Rayleigh waves.

5. Shear wave velocity inversion

5.1. *Methodology*

In section 4.2, 2-D isotropic phase and group speed maps for Rayleigh and Love waves at different periods are derived. These period-dependent isotropic phase and group speed maps can be used to infer the Vs structure. In this study, we adopt the iterative 1-D Vs inversion scheme of Herrmann (2013) to construct our final 3D shear wave velocity model for the SC plate boundary region. We use the Southern California Community Velocity Models CVM-H15.1 as our reference starting model.

In each of these 1-D Vs inversions, to avoid overshooting, we use a damping factor of 50 in the first 3 iterations, and then lower it to 5 for another 20 iterations. In the process, we fix the Vp/Vs ratio and Moho depth, and use the differential smoothing constraint to prevent unrealistic (e.g. large jumps, oscillating-like) shape in the final inverted 1-D Vs profile. Once the final inverted Vs profile is obtained, we correct the topography effect by simply subtracting the elevation value from the depth of the Vs profile and assemble all the corrected 1-D Vs profiles to construct the final pseudo-3D Vs model for the entire region. To evaluate the performance of every 1D Vs inversion, we define misfit χ as

$$\chi = \sqrt{\frac{1}{n}\sum_{i=1}^{n}\left[\left(\upsilon_i^{obs} - \upsilon_i^{pred}\right)/\sigma_i^{obs}\right]^2}\,, \tag{9}$$

where n is the number of input dispersion data points, υ_i^{obs} and υ_i^{pred} denote the input and model predicted dispersion wave speed for the i-th data point, σ_i^{obs} is the corresponding data uncertainty. A χ value less than 1 indicates, on average, the model predicted dispersion curves fit the input dispersion curves within the corresponding uncertainties. Therefore, we set a threshold of 2 to reject inverted Vs profiles with poor data fitting. In addition, we can also compute the χ value for the initial model and compare it with that of the final model to estimate the general variance reduction.

Due to the limited period range (i.e. 2.5-16s) of the input surface wave dispersion curves, the result of the inverted models can be somewhat sensitive to the reference starting model used, and this sensitivity can vary with depth. Figure 12 shows the comparison between the inverted 1-D Vs profiles obtained using CVM-H15.1 and CVM-S4.26 as the reference starting model at an example grid point near the SGP. Despite the differences in the reference starting model, the resulting misfits from both inversions are almost the same, and the inverted Vs profiles are also consistent between 3 km and 25 km, suggesting the inverted result in this depth range is well constrained by our data. However, large discrepancies are observed in the top 3 km and below the Moho, suggesting the Vs values are not well constrained beyond the 3-25 km depth range, and thus are heavily biased by the initial model. In order to further quantify how the inverted Vs values are constrained at different depths, we use an improved Neighborhood Algorithm (NA) developed by Wathelet (2008) to assess the non-uniqueness of the 1-D Vs inversion. By exploring the physical parameter space (i.e. layer thickness, Vp, Vs, and density), the NA method can find a collective of models that fits the dispersion data within a given misfit range (e.g. Sambridge, 1999). Here we use the variability of all these Vs models as a function of depth to infer the uncertainty.

Figure 13 shows an example of such exploration using NA at an example grid cell in the SGP. In the example, we parameterize the 1-D model with 7 layers (6 layers with linearly increasing Vs and flexible thickness + a bottom half space). After 200 iterations with 40,200 models being tested, we then select the series of 1-D Vs profiles with misfits less than 1.5 times the lowest misfit of all models. The surviving 1-D Vs profiles are shown as the gray shaded area in Fig. 12 and the uncertainties at each depth can be estimated as the corresponding width of the gray shaded area. Consistent with what we observed in the comparison between inverted results using different initial models (Fig. 12a), the uncertainty shows much larger values at shallow depth (i.e. top 3 km) and below 25 km. Consistent observations are seen at several other grid points that are located at some of the representative geologic provinces (Fig. S9), thus in later sections, we only focus our discussions on the depth range of 3-25 km. For the Vs structures in the top 3 km, one can defer to either the Vs model presented in Berg et al. (2018), in which shallow structure is better constrained by H/V ratio, or the geotechnical layer added in the CVM-H15.1 or CVM-S4.26.

As the Vs depth sensitivity kernels for Rayleigh wave dispersions are different from those of Love wave dispersions (Fig. S3), joint inversion of both Rayleigh and Love wave dispersion curves could imply stronger constraint in the Vs inversion. However, Rayleigh and Love wave velocity dispersions are sensitive to different Vs structures, V_{SV} and V_{SH}, respectively. Thus, following Zigone et al (2015), we only perform the Vs inversion separately for Rayleigh and Love waves to account for differences both in data quality and (apparent) radial anisotropy (Fig. S10). Considering the quality of the isotropic Rayleigh wave phase and group speed maps is much higher than those for Love waves, we only focus on the discussion of the Vs model from jointly inverting the Rayleigh wave phase and group dispersion curves, while the Vs model derived from Love wave data can be found in the supplementary material.

5.2. ***3-D shear wave velocity model***

Figure 14 summarizes results associated with the linearized 1-D Vs joint inversions using Rayleigh wave phase and group dispersion curves. The misfit corresponding to the CVM-H15.1 (Fig. 14a) and CVM-S4.26 (Fig. 14c) suggest that the surface wave dispersions predicted by the initial models are, in general, inconsistent (i.e. large χ values) with the final results obtained from the Eikonal tomography (Figs. 14b&d). The misfit distribution for the final inverted Vs models is similar regardless of which initial model is used. We prefer the final Vs model inverted using CVM-H15.1 as the initial model since: 1) Topography is considered in CVM-H15.1 but ignored in CVM-S4.26; 2) The misfit histogram suggests a slightly smaller χ value for CVM-H15.1 than CVM-S4.26; 3). Also, the 1-D Vs profiles of CVM-H15.1 are generally simpler than those of CVM-S4.26 (e.g. Fig. 12).

Map views of the final Vs model and differences from the initial model CVM-H15.1 at depths of 3 km, 5 km, 7 km, 10 km, 15 km, and 20 km are shown in Figs. 15, 16, and 17. Since the Vs inversion is performed at each individual grid node, the lateral resolution of the resulting Vs maps is comparable to those of the surface wave speed maps estimated in section 4.1 (i.e. 5-15 km near the center and 15-30 km near the edge). The largest differences are observed underneath basins, such as the Salton Trough, and part of ECSZ for depth between 3 km and 10 km. This is consistent with the fact that the χ misfit values are significantly reduced in these regions (Fig. S11). In general, we observe the following prominent features:

1). The Southern Central Valley is characterized by LVZ and it changes rapidly to high velocity Sierra Nevada foothills. This is consistent with the surface geology and previous tomographic imaging results (e.g. Tape et al., 2010; Lee et al., 2014; Berg et al., 2018).

2). The Ventura and LA basins are well confined and highlighted by the slowest velocities of the entire map in the top 3-7 km.

3). A LVZ is observed within the junction southeast to SGP between SJF and SAF.

4). Clear LVZ with a width of ~ 20 km is observed centered on the section of SAF southeast of the SGP (Fig. 17). This is consistent with results obtained by Share et al. (2019). Different from the initial model (Fig. S12), this LVZ likely reflecting fault damage is still clearly observed up to a depth of 5 km. A LVZ is also observed around the SJF in the top 5 km.

5). We observe a clear north-south oriented fast velocity block that cuts through the SGP at 5 km and 7 km depth, leading to a flipping of the velocity contrast polarity across the fast velocity anomaly. This agrees well with the observation of velocity contrast reversal across the SAF northwest and southeast of the SGP (Share & Ben-Zion, 2016),

6) The Vs around the ECSZ is much slower after the inversion, particularly for the region north to SGP for depths from 5 km to 10 km (Fig. 17), which corresponds well with the area that has large damage volume in Ben-Zion and Zaliapin (2019).

7) The Salton Trough is imaged with a well-defined shape of LVZ extended to depth 7 km in our final Vs model. Compared to the initial model, the velocities are much slower (~ 0.3 km/s) in the top 3-7 km.

8) Different from the initial model, a clear shift in the velocity contrast interface location is observed by comparing Vs at 10 km and 15 km for our final Vs model at the south SAF (Fig. 17), indicating a northeast dipping fault plane.

9) The highest velocities are observed in the Peninsular Ranges, and a sharp velocity contrast from west to east at greater depth (7-15 km; white vertical line in Fig. 17) that corresponds to the Hemet step-over (Marliyani et al., 2013) is observed much clearly in the final model.

10) Velocity contrasts across major faults (e.g. SAF, SJF) previously imaged in other tomography (e.g. Fang et al., 2016; Share et al., 2019) and fault zone head wave studies (Share and Ben-Zion, 2016, 2018) are observed clearly in the final Vs model.

Figure 18 presents Vs profiles for six cross-sections crossing the SAF at different locations from the north (AA') to south (FF'). In each profile, Vs structures between 3 km and 20 km are displayed. These cross-sections show the following features:

1) The LA basin is deeper, with a maximum depth of ~ 10 km, and larger in our final Vs model than the initial model. This is consistent with the LA basin inferred from the geology-based velocity model of Magistrale et al. (1996), which has an average depth of ~ 5 km and maximum depth of 10 km.

2) Beneath the LA basin, there is a low-velocity fault-plane-like block dipping towards the northeast.

3) The SJF is identified as a near-vertical-dipping fault in DD' centered on a localized LVZ.

4) Pronounced deep (15-20 km) low velocity body is found beneath SGP, which is likely linked to large damage volume indicated in the study of Ben-Zion and Zaliapin (2019).

5) The south SAF is found to be a localized fault associated with a velocity contrast interface and dipping to the northwest.

6) Localized LVZ with much slower (~0.2-0.3 km/s) velocities extend to 7 km beneath the ECSZ. These features are seen much more clearly in our final Vs model compared to the CVM-H15.1 (Fig. S13).

6. Discussion & Conclusions

We obtain 3-D tomographic images of S wave velocities with a grid size of 0.05º in the SC plate boundary region using Eikonal tomography (Lin et al., 2009; section 4) and 1-D linearized Vs inversion scheme (Herrmann, 2013; section 5). The study employed one year of continuous seismic data recorded on more than 300 stations in SC. The preprocessing steps discussed in Zigone et al. (2015) are first utilized to compute reliable daily ANC for every station pair throughout the year (section 2), and then phase and group travel time dispersion relations are extracted automatically from the surface waves reconstructed from all the one-year stacked cross-correlation function (section 3). The Eikonal tomography allows for rapid derivation of statistically robust and reliable isotropic Rayleigh and Love wave phase and group velocities between 2.5s and 16s. The final 3-D Vs model, with resolutions of 5-15 km in the center and 15-30 km near the edge, is inferred by jointly inverting the resulting isotropic phase and group dispersion curves through a series of 1-D linearized Vs inversions at all the grid points.

The study incorporates the following methodological improvements:

1). An automatic surface wave dispersion-picking algorithm based on frequency-time analysis is developed. To maximize the number of measurements at shorter periods (e.g. ≤ 3s) while simultaneously minimizing false detections, we perform the automatic picking procedure not only on the symmetric signals but also on both the positive and negative time lags of the correlations. Comparisons between results obtained from different components of the correlation functions help filtering out erroneous measurements identified through inconsistency.

2). The determination of phase travel time dispersion picking employs model-predicted travel time dispersion curve from the CVM-S4.26 to avoid cycle skipping (*N* in equation 2).

3). The group travel time dispersion picked using the method of several earlier studies (e.g. Barak et al., 2015; Zigone et al., 2015) is found to be sensitive to noise and has larger uncertainty. We therefore derive group traveltime dispersion using the obtained phase travel time dispersion following equation 3, which improves the accuracy of the measurements (Figs. 6d&7a).

4). In addition to the quality control criteria developed in Lin et al. (2009), we introduce station configuration error to identify regions that have unreliable gradient estimates due to poor data coverage (section 4.1; Fig. S5). This further improves the quality of the final stacked velocities.

5). We use both the phase and group dispersion curves to invert for Vs structures, which yields better inversion results (section 5.1).

6). The resolvability of the iterative 1-D Vs inversion is determined typically qualitatively using depth sensitivity kernels of surface wave velocity (Fig. S3; e.g. Zigone et al., 2015). Here we use a neighborhood algorithm (Wathelet 2008; Zigone et al., 2019) to evaluate the non-uniqueness of the inversion quantitatively. The resulting uncertainties show small values at the depth range of ~3-25km, at which the Vs profiles inverted using different initial models are consistent. This suggests that although Rayleigh wave group velocities at 3s have sufficient sensitivity and can constrain the Vs structures in the top 3 km (e.g. Barak et al., 2015; Zigone et al., 2015), the Vs values in the top 3 km from such 1-D inversion are non-unique and likely be biased by the initial model.

The resulting tomographic model of Vs using Rayleigh wave data is consistent overall with previous inferences on the large-scale velocity structure in SC (e.g. Tape et al., 2010; Allam et al., 2012; Lee et al., 2014; Zigone et al., 2015; Barak et al., 2015; Fang et al., 2016; Berg et al., 2018; Share et al., 2019). However, we find a large discrepancy between the surface wave dispersions obtained in this study and those predicted by the SCEC community velocity models, particularly for regions inside the basins and around fault zones (Figs. S11&S15). The surface wave imaging results derived in the current study provide likely better results on these structural features owing to the denser data and methodology improvements included in the current study. In addition, we observed several important features not included in the initial models including a reversed polarity of the velocity contrast across the segments of SAF that are southeast and northwest to the SGP and a northeast dipping SAF southeast to the SGP.

Comparisons between our model results and the distribution of rock damage estimated in Ben-Zion and Zaliapin (2019) from the background seismicity yields a good correlation between the LVZ and large estimated damage volumes in the ECSZ (Fig. 17) and at depths of ~15-20 km beneath the SGP (DD' of Fig. 18). The low velocity anomalies in the ECSZ seem to coincide with the rupture zones of the M6.1 Joshua Tree, M7.3 Landers, and M6.3 Big Bear earthquakes happened in 1992. The large damage volume beneath the SGP may be related (Lyakhovsky & Ben-Zion, 2009) to a significant change in Moho geometry below the South-Central Transverse Ranges (Zhu & Kanamori, 2000; Ozakin & Ben-Zion, 2015).

Compared to the initial models, our final Vs model better characterizes the fault zones in the upper crust, which are illuminated by LVZ centered on the fault surface traces in the top 3-7 km. Interestingly, the LVZ underneath the SJF is less significant compared to initial models, particularly beneath the trifurcation area, suggesting the area may not be as localized as the south SAF. In addition, we observe a low velocity strip beneath the LA basin dipping northward to ~15 km depth with an angle of ~30º (CC' of Fig. 18). The estimated surface location, dipping direction and angle, and depth range of the low velocity strip coincide with features of the Puente Hills blind-thrust system imaged by Shaw et al. (2002). The estimated ~3-5% velocity reduction of the low velocity strip compared to the surrounding structures (CC' of Fig. 18) is consistent with the fact that the Puente Hills blind-thrust system is capable of generating Mw6.0+ earthquake (Shaw et al., 2002).

The results from noise-based Eikonal tomography significantly improve the fitting of the Rayleigh wave dispersion measurements (Fig. 14) by updating the Vs structures in the top 3-20 km for the southern California plate boundary region, particularly near fault surface traces. To obtain reliable Vs structures in the top 3 km, either surface wave velocity dispersion at higher frequencies (e.g. > 1 Hz; Lin et al., 2013) or joint inversion with other types of measurements such as Rayleigh wave H/V ratio (e.g. Berg et al., 2018) are required. Our new model shows more detailed features in the upper crust (section 5.2) than the initial models; however, the results should be validated by comparing synthetic waveforms using this model to ANC or recordings of local earthquakes (e.g. Ma et al., 2008; Taborda et al., 2016; Fang et al., 2016). In addition, the final 3-D velocity model is constructed based on a two-step inversion scheme and the assumption that the amplitude field is sufficiently smooth. This implies that the model may not perform well in explaining earthquake waveforms recorded around and inside basins, which can potentially be improved by using the Helmholtz tomography (equation 4b).

The final Vs model using Love wave data is shown in Figs. S14-S19. Consistent features in the Vs structures are observed, including as misfit histogram and distribution (Figs. S14&S15), localized LVZ in the top 5 km related to fault damage (Fig. S16), fault-like-structure with a dipping angle of ~30º beneath LA basin, and prominent low velocity body located between 15-20 km depth beneath SGP (Fig. S17). Some discrepancies are found between the derived Vs models from Rayleigh and Love waves, such as the observation of dipping SAF is clear in the Rayleigh wave results (EE' & FF' in Fig. 18) but not in those of Love waves (Fig. S18). These differences appear to be quite large particularly below 7 km. Since a non-negligible ray bending is observed in the surface wave propagation (e.g. Fig. 9), the transverse component of the ANC is no longer normal to the interstation path; a correction in the TT tensor rotation may result in a smaller discrepancy between results using Rayleigh and Love waves. The observed differences between imaging results using data from Rayleigh and Love waves suggest the existence of significant apparent radial anisotropy, which may be caused by transverse isotropy (e.g. Moschetti et al., 2010a) or 3D structural effects (e.g. Levshin & Ludmila Ratnikova, 1984). The radial and 2-psi azimuthal anisotropy can provide additional information on crustal properties (e.g. Moschetti et al., 2010b; Lin et al., 2011) in the study region and will be the subject of a future study.

Acknowledgements:

The seismic data used in this work were obtained from the Southern California Earthquake Data Center [*SCEDC,* 2013] and the IRIS Earthquake Data Center (https://ds. iris.edu/ds/nodes/dmc/). Both the SCEC Community Velocity Models, CVMS-4.26 and CVMH-15.1.0, used in this work are available from the Southern California Earthquake Center (https://github.com/ SCECcode/UCVMC). The study was supported by the Earthquake Hazards Program of the USGS (grant G16AP00105) and the National Science Foundation (grant EAR-1841315). We thank the reviewers C. Tape and M. Denolle, the Associate Editor N. Nakata, and the Editor M. Savage for comments that helped to improve the manuscript. The 3-D Vs model will be available from IRIS Data Services Products: Earth Model Collaboration (https://ds.iris.edu/ds/products/emc/).

References

Aki, K., & Richards, P. G. (2002). Quantitative seismology (2nd ed.). Mill Valley, CA: University Science Books.

Allam, A. A., & Ben-Zion, Y. (2012). Seismic velocity structures in the southern California plate-boundary environment from double-difference tomography. *Geophysical Journal International*, *190*(2), 1181-1196, doi:10.1111/j.1365-246X.2012.05544.x.

Allam, A. A., Ben-Zion, Y., Kurzon, I., & Vernon, F. (2014). Seismic velocity structure in the Hot Springs and Trifurcation areas of the San Jacinto fault zone, California, from double-difference tomography. *Geophysical Journal International*, *198*(2), 978-999, doi:10.1093/gji/ggu176.

Alvizuri, C., & Tanimoto, T. (2011). Azimuthal anisotropy from array analysis of Rayleigh waves in Southern California. *Geophysical Journal International*. doi:10.1111/j.1365-246X.2011.05093.x

Barak, S., Klemperer, S. L., & Lawrence, J. F. (2015). San Andreas Fault dip, Peninsular Ranges mafic lower crust and partial melt in the Salton Trough, Southern California, from ambient-noise tomography. *Geochemistry, Geophysics, Geosystems*, *16*(11), 3946-3972, doi:10.1002/2015gc005970.

Barmin, M. P., Ritzwoller, M. H., & Levshin, A. L. (2001). A Fast and Reliable Method for Surface Wave Tomography. *Pure and Applied Geophysics*. *158*, 1351-1375.

Ben-Zion, Y. & Zaliapin, I. (2019). Spatial variations of rock damage production by earthquakes in southern California. *Earth Planet. Sci. Lett.,* 512, 184–193, doi: 10.1016/j.epsl.2019.02.006.

Bensen, G. D., Ritzwoller, M. H., Barmin, M. P., Levshin, A. Lin, F. C., Moschetti, M. P., Shapiro, N. M., & Yang, Y. (2007). Processing seismic ambient noise data to obtain reliable broad-band surface wave dispersion measurements. *Geophysical Journal International*, *169*(3), 1239-1260, doi:10.1111/j.1365-246X.2007.03374.x.

Berg, E. M., Lin, F. C., Allam, A., Qiu, H., Shen, W., & Ben-Zion, Y. (2018). Tomography of Southern California Via Bayesian Joint Inversion of Rayleigh Wave Ellipticity and Phase Velocity From Ambient Noise Cross-Correlations. *Journal of Geophysical Research: Solid Earth*, *123*(11), 9933-9949, doi:10.1029/2018jb016269.

Boué, P., P. Roux, Campillo, M., & Cacqueray, B. d. (2013). Double beamforming processing in a seismic prospecting context. *GEOPHYSICS*, *78*(3), V101-V108, doi:10.1190/GEO2012-0364.1.

Boúe, P., Denolle, M., Hirata, N., Nakagawa, S., & Beroza, G. C. (2016). Beyond basin resonance : Characterizing wave propagation using a dense array and the ambient seismic field. *Geophysical Journal International*. doi:10.1093/gji/ggw205

California Institute of Technology and United States Geological Survey Pasadena (1926): Southern California Seismic Network. International Federation of Digital Seismograph Networks. Dataset/Seismic Network. 10.7914/SN/CI

Fang, H., Zhang, H., Yao, H., Allam, A., Zigone, D., Ben-Zion, Y., et al. (2016). A new algorithm for three-dimensional joint inversion of body wave and surface wave data and its application to the Southern California plate boundary region. *Journal of Geophysical Research: Solid Earth*, *121*(5), 3557-3569, doi:10.1002/2015jb012702.

Gouédard, P., Yao, H., Ernst, F., & van der Hilst, R. D. (2012). Surface wave eikonal tomography in heterogeneous media using exploration data. *Geophysical Journal International*, *191*(2), 781-788, doi:10.1111/j.1365-246X.2012.05652.x.

Hauksson, E., Yang, W., & Shearer, P. M. (2012). Waveform Relocated Earthquake Catalog for Southern California (1981 to June 2011). *Bulletin of the Seismological Society of America*, *102*(5), 2239-2244, doi:10.1785/0120120010.

Herrmann, R. B. (2013). Computer Programs in Seismology: An Evolving Tool for Instruction and Research. *Seismological Research Letters*, *84*(6), 1081-1088, doi:10.1785/0220110096.

Hillers, G., Ben-Zion, Y., Landès, M., & Campillo, M. (2013). Interaction of microseisms with crustal heterogeneity: A case study from the San Jacinto fault zone area. *Geochemistry, Geophysics, Geosystems*, *14*(7), 2182-2197, doi:10.1002/ggge.20140.

Kedar, S., & Webb, F. H. (2005). The Ocean's Seismic Hum. *Science*, 307, doi:10.1126/science.1108380.

Lee, E.-J., Chen, P., Jordan, T. H., Maechling, P. B., Denolle, M. A. M., & Beroza, G. C. (2014). Full-3-D tomography for crustal structure in Southern California based on the scattering-integral and the adjoint-wavefield methods. *Journal of Geophysical Research: Solid Earth*, *119*(8), 6421-6451, doi:10.1002/2014jb011346.

Lévěque, J. J., Rivera, L., & Wittlinger, G. (1993). On the use of the checker-board test to assess the resolution of tomographic inversions. *Geophysical Journal International*, *115*(1), 313-318.

Li, Y., Wu, Q., Pan, J., & Sun, L. (2012). S-wave velocity structure of northeastern China from joint inversion of Rayleigh wave phase and group velocities. *Geophysical Journal International*, *190*(1), 105-115.

Lin, F.-C., Li, D., Clayton, R. W., & Hollis, D. (2013). High-resolution 3D shallow crustal structure in Long Beach, California: Application of ambient noise tomography on a dense seismic array. *Geophysics*, *78*(4), Q45-Q56, doi:10.1190/GEO2012-0453.1.

Lin, F.-C., & Ritzwoller, M. H. (2011). Helmholtz surface wave tomography for isotropic and azimuthally anisotropic structure. *Geophysical Journal International*, *186*(3), 1104-1120, doi:10.1111/j.1365-246X.2011.05070.x.

Lin, F.-C., & Schmandt, B. (2014). Upper crustal azimuthal anisotropy across the contiguous U.S. determined by Rayleigh wave ellipticity. *Geophysical Research Letters*, *41*(23), 8301-8307, doi:10.1002/2014gl062362.

Lin, F. C., Ritzwoller, M. H., Townend, J., Bannister, S., & Savage, M. K. (2007). Ambient noise Rayleigh wave tomography of New Zealand. *Geophysical Journal International*, *170*(2), 649-666.

Lin, F.-C., Moschetti, M. P., & Ritzwoller, M. H. (2008). Surface wave tomography of the western United States from ambient seismic noise: Rayleigh and Love wave phase velocity maps. *Geophysical Journal International*, *173*(1), 281-298, doi:10.1111/j.1365-246X.2008.03720.x.

Lin, F.-C., Ritzwoller, M. H., & Snieder, R. (2009). Eikonal tomography: surface wave tomography by phase front tracking across a regional broad-band seismic array. *Geophysical Journal International*, *177*(3), 1091-1110, doi:10.1111/j.1365-246X.2009.04105.x.

Lobkis, O. I., & Weaver, R. L. (2001). On the emergence of the Green's function in the correlations of a diffuse field. *The Journal of the Acoustical Society of America*, *110*, doi:10.1121/1.1417528.

Lyakhovsky, V., & Ben-Zion, Y. (2009). Evolving geometrical and material properties of fault zones in a damage rheology model. *Geochemistry, Geophysics, Geosystems*, *10*(11), n/a-n/a, doi:10.1029/2009gc002543.

Ma, S., Prieto, G. A., & Beroza, G. C. (2008). Testing community velocity models for southern California using the ambient seismic field. *Bulletin of the Seismological Society of America*. doi:10.1785/0120080947

Ma, Y., Clayton, R. W., & Li, D. (2016). Higher-mode ambient-noise Rayleigh waves in sedimentary basins. *Geophysical Journal International*. doi:10.1093/gji/ggw235

Marliyani, G. I., Rockwell, T. K., Onderdonk, N. W., & McGill, S. F. (2013). Straightening of the Northern San Jacinto Fault, California, as Seen in the Fault-Structure Evolution of the San Jacinto Valley Stepover. *Bulletin of the Seismological Society of America*, *103*(3), 2047-2061, doi:10.1785/0120120232.

Moschetti, M. P., Ritzwoller, M. H., Lin, F. C., & Yang, Y. (2010a). Crustal shear wave velocity structure of the western United States inferred from ambient seismic noise and earthquake data. *Journal of Geophysical Research: Solid Earth*, *115*(B10).

Moschetti, M. P., Ritzwoller, M. H., Lin, F., & Yang, Y. (2010b). Seismic evidence for widespread western-US deep-crustal deformation caused by extension. *Nature*, *464*(7290), 885.

Ozakin, Y., & Ben-Zion, Y. (2015). Systematic Receiver Function Analysis of the Moho Geometry in the Southern California Plate-Boundary Region. *Pure and Applied Geophysics*, *172*(5), 1167-1184, doi:10.1007/s00024-014-0924-6.

Poli, P., Pedersen, H. A., Campillo, M., & POLENET/LAPNET Working Group. (2012). Noise directivity and group velocity tomography in a region with small velocity contrasts: the northern Baltic shield. *Geophysical Journal International*, *192*(1), 413-424.

Prindle, K., & Tanimoto, T. (2006). Teleseismic surface wave study for S-wave velocity structure under an array: Southern California. *Geophysical Journal International*. doi:10.1111/j.1365-246X.2006.02947.x

Qin, L., Ben-Zion, Y., Qiu, H., Share, P. E., Ross, Z. E., & Vernon, F. L. (2018). Internal structure of the San Jacinto fault zone in the trifurcation area southeast of Anza, California, from data of dense seismic arrays. *Geophysical Journal International*, *213*(1), 98-114.

Qiu, H., Ben-Zion, Y., Ross, Z. E., Share, P. E., & Vernon, F. L. (2017). Internal structure of the San Jacinto fault zone at Jackass Flat from data recorded by a dense linear array. *Geophysical Journal International*, *209*(3), 1369-1388.

Ritzwoller, M. H., Lin, F. C., & Shen, W. (2011). Ambient noise tomography with a large seismic array. *Comptes Rendus Geoscience*, *343*(8-9), 558-570.

Roux, P., & Ben-Zion, Y. (2017). Rayleigh phase velocities in Southern California from beamforming short-duration ambient noise. *Geophysical Journal International*, *211*(1), 450-454, doi:10.1093/gji/ggx316.

Roux, P., Sabra, K. G., Kuperman, W. A., & Roux, A. (2005). Ambient noise cross correlation in free space: Theoretical approach. *The Journal of the Acoustical Society of America*, *117*(1), 79-84.

Sabra, K. G., Roux, P., & Kuperman, W. A. (2005). Emergence rate of the time-domain Green's function from the ambient noise cross-correlation function. *The Journal of the Acoustical Society of America*, *118*, doi:10.1121/1.2109059.

Sambridge, M. (1999). Geophysical inversion with a neighbourhood algorithm - I. Searching a parameter space. *Geophysical Journal International*. doi:10.1046/j.1365-246X.1999.00876.x

Savage, M. K., Lin, F. C., & Townend, J. (2013). Ambient noise cross-correlation observations of fundamental and higher-mode Rayleigh wave propagation governed by basement resonance. *Geophysical Research Letters*. doi:10.1002/grl.50678

SCEDC (2013). Southern California Earthquake Center. Caltech. Dataset. doi:10.7909/C3WD3xH1

Sethian, J. A. (1996). A fast marching level set method for monotonically advancing fronts. *Proceedings of the National Academy of Science*, *93*, 1591-1595.

Shapiro, N. M., & Campillo, M. (2004). Emergence of broadband Rayleigh waves from correlations of the ambient seismic noise. *Geophysical Research Letters*, *31*(7), n/a-n/a, doi:10.1029/2004gl019491.

Shapiro, N. M., Campillo, M., Stehly, L., & Ritzwoller, M. H. (2005). High-resolution surface-wave tomography from ambient seismic noise. *Science*, *307*(5715), 1615–1618. doi:10.1126/science.1108339

Share, P.-E., & Ben-Zion, Y. (2016). Bimaterial interfaces in the south San Andreas Fault with opposite velocity contrasts NW and SE from San Gorgonio Pass. *Geophysical Research Letters*, doi:10.1002/2016GL070774.

Share, P.-E. & Ben-Zion, Y. (2018). A bimaterial interface along the northern San Jacinto fault through Cajon Pass. *Geophys. Res. Lett.*, 45, 11,622–11,631, doi: 10.1029/2018GL079834.

Share, P. E., Ben-Zion, Y., Ross, Z. E., Qiu, H., & Vernon, F. L. (2017). Internal structure of the San Jacinto fault zone at Blackburn Saddle from seismic data of a linear array. *Geophysical Journal International*, *210*(2), 819-832.

Share, P. E., Guo, H., Thurber, C. H., Zhang, H., & Ben-Zion, Y. (2019). Seismic Imaging of the Southern California Plate Boundary around the South-Central Transverse Ranges Using Double-Difference Tomography. *Pure and Applied Geophysics*, *176*(3), 1117-1143.

Shaw, J. H., Plesch, A., Dolan, J. F., Pratt, T. L., & Fiore, P. (2002). Puente Hills Blind-Thrust System, Los Angeles, California. *Bulletin of the Seismological Society of America*, *92*(8), 2946-2960.

Shaw, J. H., Plesch, A., Tape, C., Suess, M. P., Jordan, T. H., Ely, G., et al. (2015). Unified structural representation of the southern California crust and upper mantle. *Earth and Planetary Science Letters*, 415, 1–15. https://doi.org/10.1016/j.epsl.2015. 01.016

Smith, W. H. F., & Wessel, P. (1990). Gridding with continuous curvature splines in tension. *Geophysics*, *55*(3), 293-305.

Snieder, R. (2004). Extracting the Green's function from the correlation of coda waves: a derivation based on stationary phase. *Physical review. E, Statistical, nonlinear, and soft matter physics*, *69*(4 Pt 2), 046610, doi:10.1103/PhysRevE.69.046610.

Taborda, R., Azizzadeh-Roodpish, S., Khoshnevis, N., & Cheng, K. (2016). Evaluation of the southern California seismic velocity models through simulation of recorded events. *Geophysical Journal International*. doi:10.1093/gji/ggw085

Tape, C., Liu, Q., Maggi, A., & Tromp, J. (2010). Seismic tomography of the southern California crust based on spectral-element and adjoint methods. *Geophysical Journal International*, *180*(1), 433-462, doi:10.1111/j.1365-246X.2009.04429.x.

Vernon, F. L. (1982). ANZA Regional Network. San Diego: International Federation of Digital Seismograph Networks. doi: doi.org/10.7914/SN/AZ

Vernon, F. L., & Ben-Zion, Y. (2010). San Jacinto Fault Zone Experiment Network. Inter national Federation of Digital Seismograph Networks. doi: https://doi.org/10.7914/ SN/YN 2010

Wathelet, M. (2008). An improved neighborhood algorithm: Parameter conditions and dynamic scaling. *Geophysical Research Letters*, *35*(9), doi:10.1029/2008gl033256.

Wielandt, E. (1993). Propagation and structural interpretation of non-plane waves. *Geophysical Journal International*, *113*, 45-53.

Xu, H., Luo, Y., Chen, C., & Xu, Y. (2016). 3D shallow structures in the Baogutu area, Karamay, determined by eikonal tomography of short-period ambient noise surface waves. *Journal of Applied Geophysics*, *129*, 101-110.

Yang, Y., & Forsyth, D. W. (2006). Rayleigh wave phase velocities, small-scale convection, and azimuthal anisotropy beneath southern California. *Journal of Geophysical Research: Solid Earth*, *111*(7), 1–20. doi:10.1029/2005JB004180

Yao, H., & van der Hilst, R. D. (2009). Analysis of ambient noise energy distribution and phase velocity bias in ambient noise tomography, with application to SE Tibet. *Geophysical Journal International*, *179*(2), 1113-1132, doi:10.1111/j.1365-246X.2009.04329.x.

Zhu, L., & Kanamori, H. (2000). Moho depth variation in southern California from teleseismic receiver functions. *Journal of Geophysical Research: Solid Earth*, *105*(B2), 2969-2980, doi:10.1029/1999jb900322.

Zigone, D., Ben-Zion, Y., Campillo, M., & Roux, P. (2015). Seismic tomography of the Southern California plate boundary region from noise-based Rayleigh and Love waves. *Pure and Applied Geophysics*, *172*(5), 1007-1032.

Zigone, D., Ben-Zion, Y., Lehujeur, M., Campillo, M., Hillers, G., & Vernon, F. L. (2019). Imaging subsurface structures in the San Jacinto fault zone with high frequency noise recorded by dense linear arrays. *Geophysical Journal International*, 217, 879–893, doi: 10.1093/gji/ggz069.

Figure Captions

Figure 1. Location map of 346 (299 three-component sensor in red) seismic stations (triangles) used for imaging the Southern California (SC) plate boundary region. Ambient noise cross-correlations (ANC) computed at two example station pairs (green lines) are shown in Fig. 3. The green square shows the location of the grid point used in Fig. 12. Surface traces of large faults together with the state and national boundaries are shown as black lines. Localities of the major faults and geologic provinces in SC are labeled. Cross sections of the final inverted shear wave velocities (Vs) are shown for the blue lines crossing San Andreas Fault at various locations in Fig. 18.

Figure 2. Flow chart of the procedures to obtain shear wave velocity model using Rayleigh waves extracted from the vertical-vertical (ZZ) component one-year stacked ANC. Same process can be applied to Love waves extracted from transverse-transverse (TT) component data.

Figure 3. Daily ANC for the entire year 2014 computed at Vertical – Vertical (ZZ) component of the (a) coast-parallel pair DJJ–GOR and (b) coast perpendicular pair GSC–SDD. Red, green and blue represent positive, zero and negative amplitude values, respectively. The black dashed lines outline Rayleigh wave signals at both positive and negative time lags. (c) One year stacked cross-correlation at components of ZZ, TT, RR, ZR, ZT, and RT computed at station pair DJJ-GOR. (d) Same as (c) for pair GSC-SDD. Noise source directionality is clearly observed in both pairs and for all components as evidenced from differences in negative and positive time lags of the ANC.

Figure 4. The top black trace shows the one-year stacked ZZ component correlation function recorded at station pair GSC-SDD. The corresponding symmetric signal, by folding and averaging (FA) the positive and negative time lags, is displayed in red. The symmetric signal is then filtered at periods 2s, 3s, 5s, 7s, 10s, 15s, and 20s, and the filtered waveform and corresponding envelope are shown in blue and black, respectively. The surface wave window is defined as an average velocity range of 1.5 km/s to 4.5 km/s, whereas an average velocity less than 1.5 km/s outlines the noise window. Signal to noise ratio (SNR) is calculated for each envelope global peak (red star). Reference phase traveltime dispersion calculated using the

CVM-S4.26 is illustrated as the red dashed curve. The blue star shows the location of a local maximum of the envelope filtered at 2s.

Figure 5. Example of frequency-time analysis performed on the symmetric correlation function shown in Fig. 4. (a). The symmetric correlation (black) is first tapered using a window bounded by the moveout range of 4 km/s and 1.5 km/s. (b) The waveform after tapering and filtering using a Gaussian narrow bandpass filter centered at period 7s is denoted by the blue signal. Phase and envelope functions are calculated and shown in red and black, respectively. The white star indicates the envelope peak with the corresponding travel time showing as green dashed lines. (c) Frequency-time diagram. After applying a series of Gaussian narrow bandpass filters centered on periods from 2s to 20s on the tapered signal shown in (a), envelope functions are arranged by the corresponding center periods. The amplitudes are illustrated as colors from blue to red indicating values from 0 to the maximum. The envelope shown in (b) is depicted at the white dashed lines. The red dashed curve denotes the reference phase traveltime dispersion curve calculated using model CVM-S4.26. Local and global maximums of all the envelope functions are shown as symbols of black plus & green circles, and red circles, respectively. Here we discard any envelope maximums (black plus) that are below the black dashed lines.

Figure 6. Rayleigh wave group and phase travel time dispersion results for example station pair GSC-SDD. (a) The black solid curve represents the group travel time dispersions measured using waveform at the symmetric signal. The corresponding phase travel time dispersion is shown as the red solid curve. The blue dashed curve represents the model predicted phase travel time dispersion using CVM-S4.26. Phase travel time dispersions with one cycle skipped (N=N_0±1 in eq. 2; red dashed curves) are shown for visual comparison. (b) Same as (a) measured at the negative time lag. (c) Same as (a) using the positive time lag. (d) Comparison of all the group (black dashed) and phase (red dashed) dispersion results. The blue and green solid curves represent the final phase and group dispersion measurements.

Figure 7. Derivation of group traveltime dispersion curve for Rayleigh waves. Panel on the left shows the measured phase traveltime dispersion curve (solid blue curve in Fig. 6d) in term of average velocity as red dots. A 1-D Vs inversion is performed to fit the phase dispersion starting with the 1-D Vs profile (black curve in the right panel) averaged over the entire CVM-S4.26 as the initial model. The phase dispersion curve (red curve in left panel) of the best fitting 1-D Vs

profile (red curve in right panel) gives the smoothed phase dispersion curve, and the corresponding group dispersion (black curve in the left panel) is calculated following equation 3.

Figure 8. Histograms of phase (blue) and group (orange) travel time measurements for Rayleigh (top panels) and Love (bottom panels) waves at 3s (left panels), 7s (middle panels), and 11s (right panels). The total number of the travel time measurements for each histogram is indicated as well.

Figure 9. Eikonal phase velocity maps computed at period 7s by using stations (a) GOR, (b) GSC, (c) IRM, and (d) OLI as the virtual source. Azimuths of the gradient are illustrated with arrows.

Figure 10. Isotropic phase velocities (a-c) and corresponding uncertainty distributions (d-f) of Rayleigh waves at 3s, 7s, 11s.

Figure 11. Same as Fig. 10 for isotropic Rayleigh wave group velocity.

Figure 12. (a) Illustration of the iterative 1-D Vs inversion of Herrmann (2013) at an example grid cell in San Gorgonio Pass located at -117°, 34°. The left panel shows the comparison between the Rayleigh wave group (in blue) and phase (in red) velocity dispersion measurements (solid circles) and the best fitting results (solid curves). The error bar indicates the uncertainty estimated from eikonal tomography (eq. 8b). Rayleigh wave dispersion curves of the initial model are also displayed as dashed curves. The χ misfit values for both the initial and best fitting 1-D Vs profiles are indicated at the top left corner. The black and red curves in the right panel denote the initial (CVM-H15.1) and best fitting 1-D Vs models. An estimation of non-uniqueness of the 1-D inversion is illustruated by the gray shaded area given by Fig. 13d. The depth dependent width of the gray shaded area is indicative of the inversion uncertainty and shown as the gray curve. (b) Same as (a) for using CVM-S4.26 as the initial model. The blue curve in the right panel represents the best fitting 1-D Vs profile obtained in (a).

Figure 13. Illustration of Neighborhood Algorithm (Wathelet, 2008) inversion results. The 1-D Vp and Vs profiles explored in the inversion are colored according to their misfit, and those with misfit values less than 1.46 are shown in (a) and (b). The corresponding group and phase velocity dispersion curves are displayed in (c) and (d). Models with misfit larger than 1.5 times

the minimum misfit value (i.e. 0.41) are discarded, and the minimum and maximum of all the acceptable 1-D Vs profiles at different depth depict the gray shaded area shown in Fig. 12.

Figure 14. Histograms of probability (in gray; PDF) and cumulative (blue curve; CDF) density distributions for χ misfit. (a) χ misfit values computed for CVM-H15.1 following equation 9 for all available grid cells. (b) Same as (a) for the best fitting Vs model using CVM-H15.1 as the initial model. (c) Same as (a) for CVM-S4.26. (d) Same as (a) for the besting fitting Vs model using CVM-S4.26 as the initial model. The corresponding spatial distributions of the χ misfit values are shown in Fig. S11.

Figure 15. Left panels show map view of the final inverted Vs model at 3 km (top), 5 km (middle), and 7 km (bottom) depths. The Vs model within the black box (top left panel) are displayed using a narrower color palette in Fig. 17. Model CVM-H15.1 is used as the initial model here, and the right panels illustrate the differences in Vs between the final and initial Vs models at 3 km, 5 km, and 7 km depths. See Figure S12 for corresponding Vs maps of the initial model.

Figure 16. Same as Fig. 15 at depths of 10 km (top), 15 km (middle), and 20 km (bottom).

Figure 17. Zoom in of Vs maps for regions near SJF and SAF (black box in left top panel of Fig. 15) at depths 3 km (top left), 5 km (middle left), 7 km (bottom left), 10 km (top right), 15 km (middle right), and 20 km (bottom right). The white ellipses outline the major features (i.e. low velocity anomaly and velocity contrast) that are more prominent in the final Vs model than the initial model.

Figure 18. Cross sections of the final inverted Vs model at locations indicated as blue lines in Fig. 1. Localities of major faults, basins, and geomorphic provinces are labeled on the top topography curve. The red dashed lines beneath LA basin at profile CC' denote a linear low velocity zone that is likely associated with the Puente Hills blind-thrust system (Shaw et al., 2002). In addition, a deep low velocity anomaly outlined by the black dashed circle at profile DD' may be related to the large damage volume estimated in Ben-Zion & Zaliapin (2019). The black dashed lines at cross sections DD', EE', and FF' denote the potential fault planes of SAF

or SJF. See Figure S13 for corresponding cross sections of the initial model (CVM-H) and the perturbations.

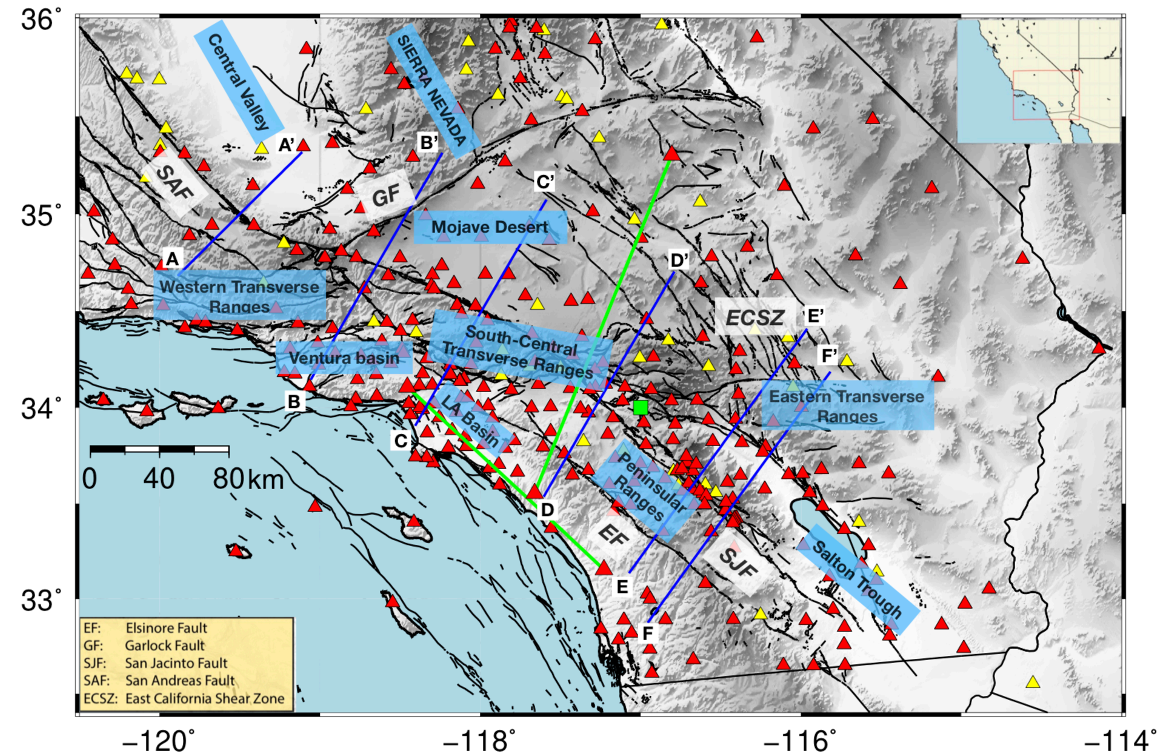
36˚
35˚
34˚
33˚
−120˚
−118˚
−116˚
−114˚
Central Valley
SIERRA NEVADA
SAF
GF
Mojave Desert
Western Transverse Ranges
Ventura basin
South-Central Transverse Ranges
LA Basin
Peninsular Ranges
EF
SJF
ECSZ
Eastern Transverse Ranges
Salton Trough
A
A'
B
B'
C
C'
D
D'
E
E'
F
F'
0
40
80 km
EF: Elsinore Fault
GF: Garlock Fault
SJF: San Jacinto Fault
SAF: San Andreas Fault
ECSZ: East California Shear Zone

Figure 1

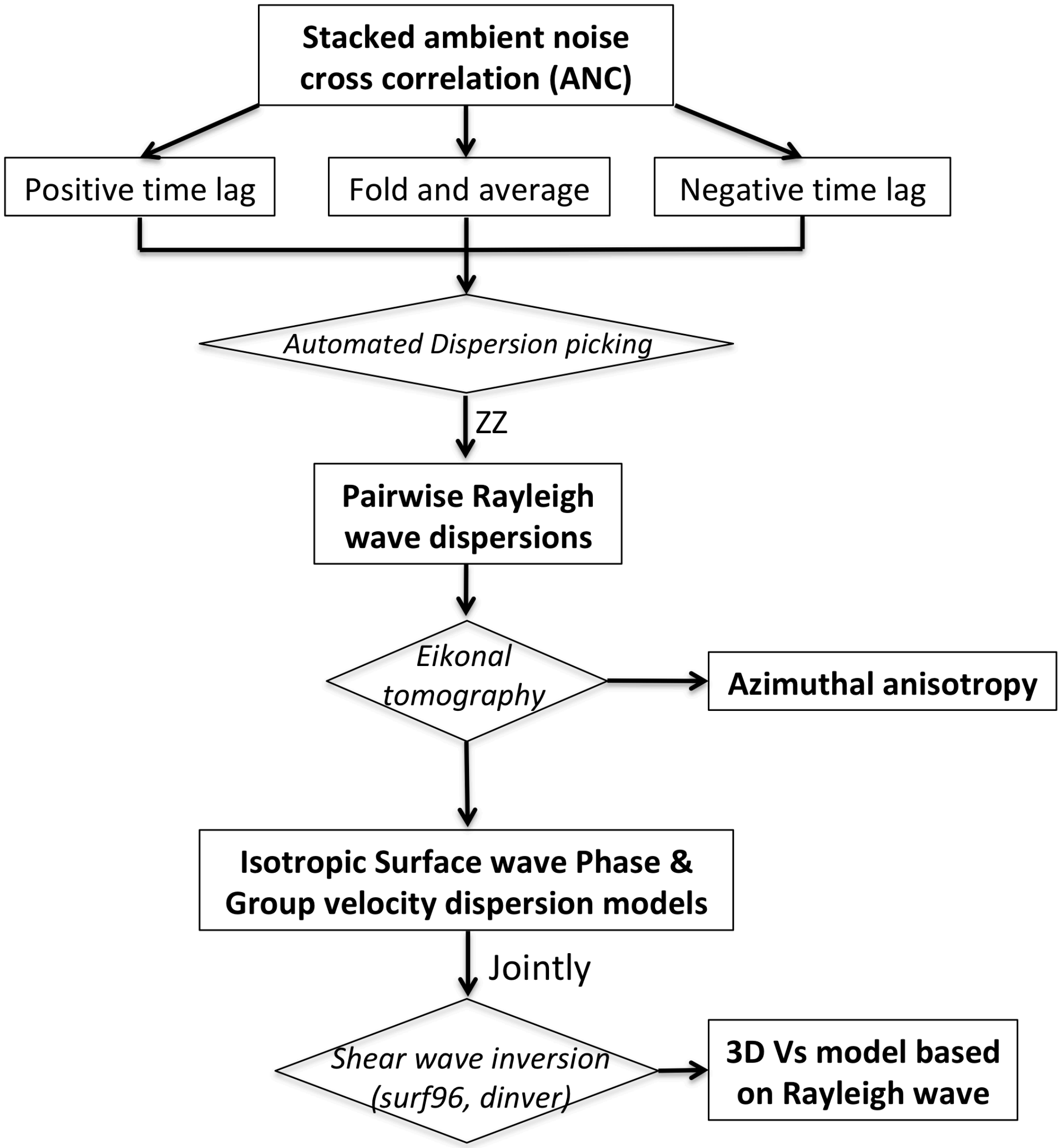
Stacked ambient noise cross correlation (ANC)
Positive time lag
Fold and average
Negative time lag
Automated Dispersion picking
ZZ
Pairwise Rayleigh wave dispersions
Eikonal tomography
Azimuthal anisotropy
Isotropic Surface wave Phase & Group velocity dispersion models
Jointly
Shear wave inversion (surf96, dinver)
3D Vs model based on Rayleigh wave

Figure 2

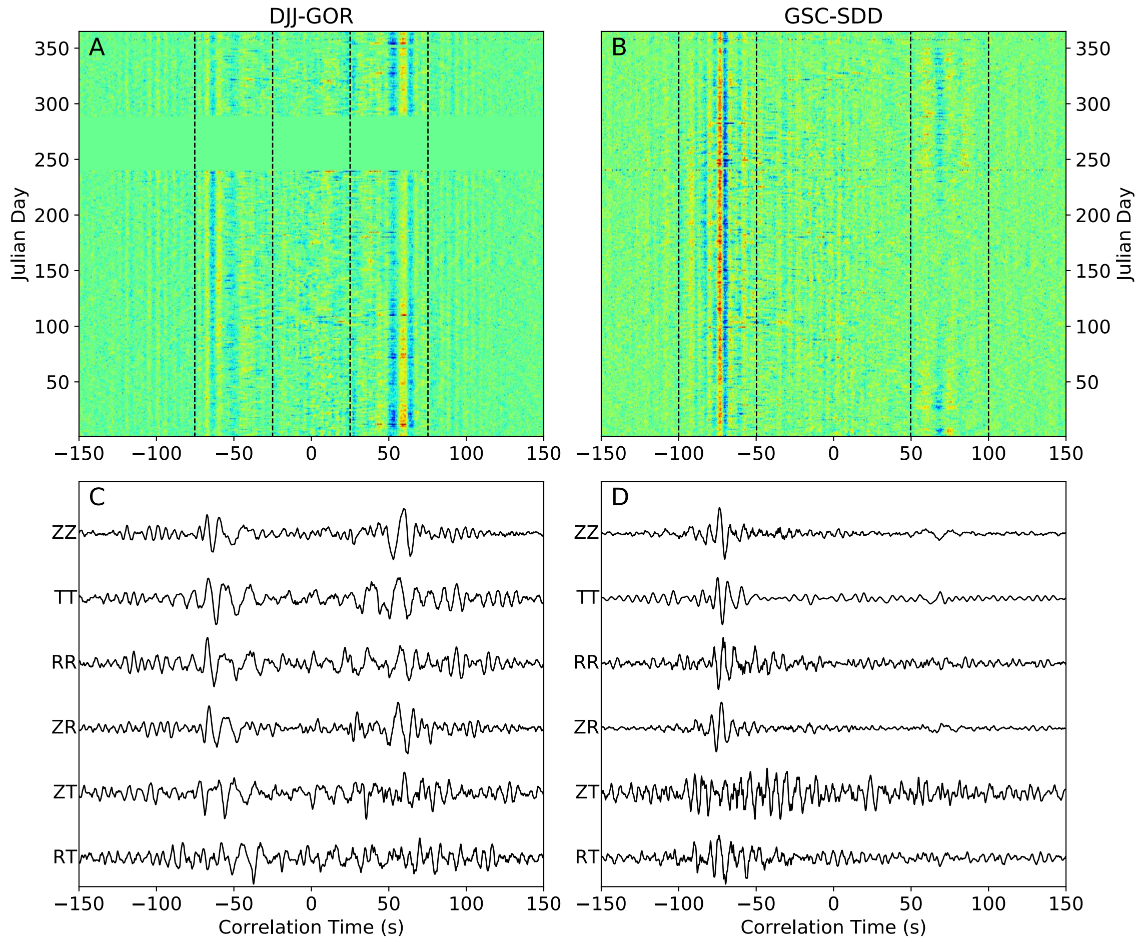

DJJ-GOR
GSC-SDD
A
B
C
D
Julian Day
350
300
250
200
150
100
50
−150
−100
−50
0
50
100
150
ZZ
TT
RR
ZR
ZT
RT
Correlation Time (s)

Figure 3

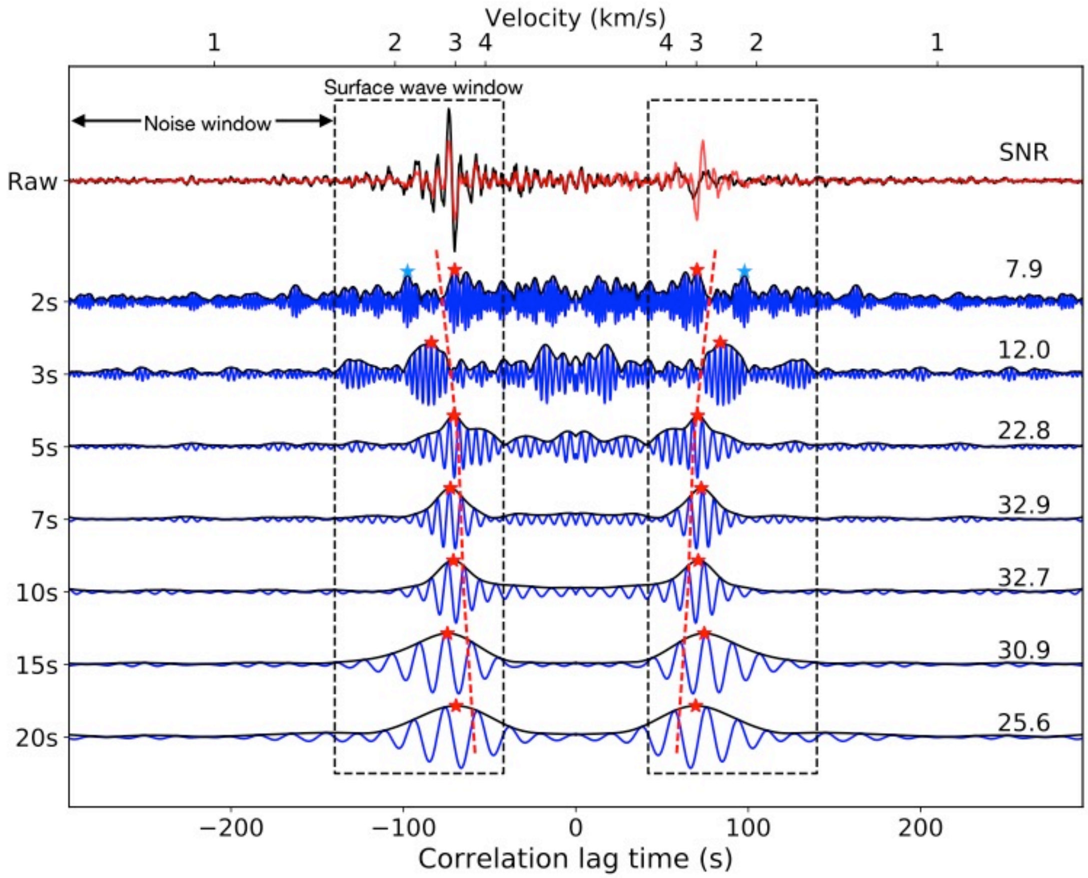
Velocity (km/s)
1
2
3
4
4
3
2
1
Surface wave window
Noise window
SNR
Raw
2s
7.9
3s
12.0
5s
22.8
7s
32.9
10s
32.7
15s
30.9
20s
25.6
−200
−100
0
100
200
Correlation lag time (s)

Figure 4

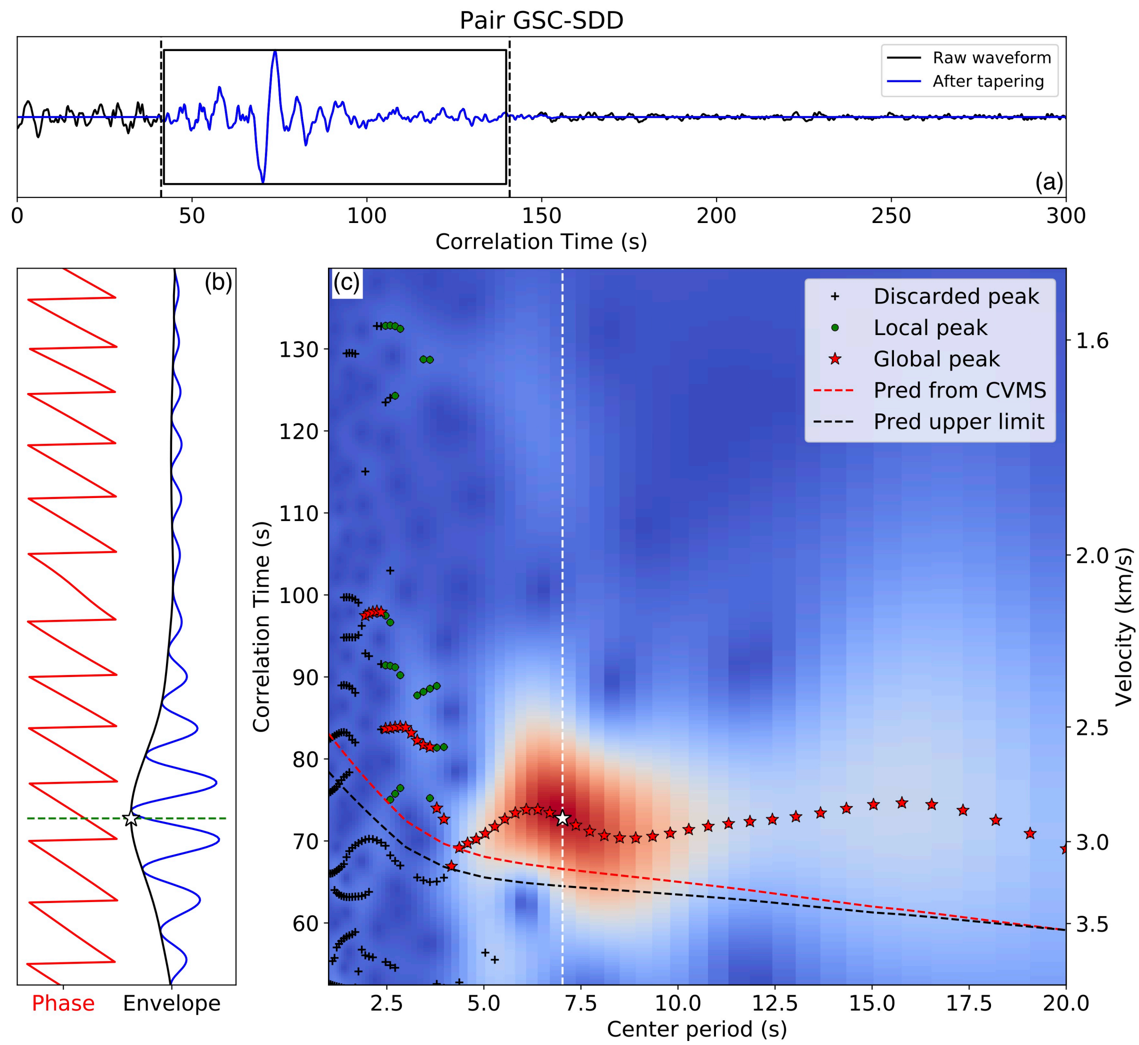

Pair GSC-SDD
Raw waveform
After tapering
(a)
0
50
100
150
200
250
300
Correlation Time (s)
(b)
Phase
Envelope
(c)
Discarded peak
Local peak
Global peak
Pred from CVMS
Pred upper limit
130
120
110
100
90
80
70
60
Correlation Time (s)
1.6
2.0
2.5
3.0
3.5
Velocity (km/s)
2.5
5.0
7.5
10.0
12.5
15.0
17.5
20.0
Center period (s)

Figure 5

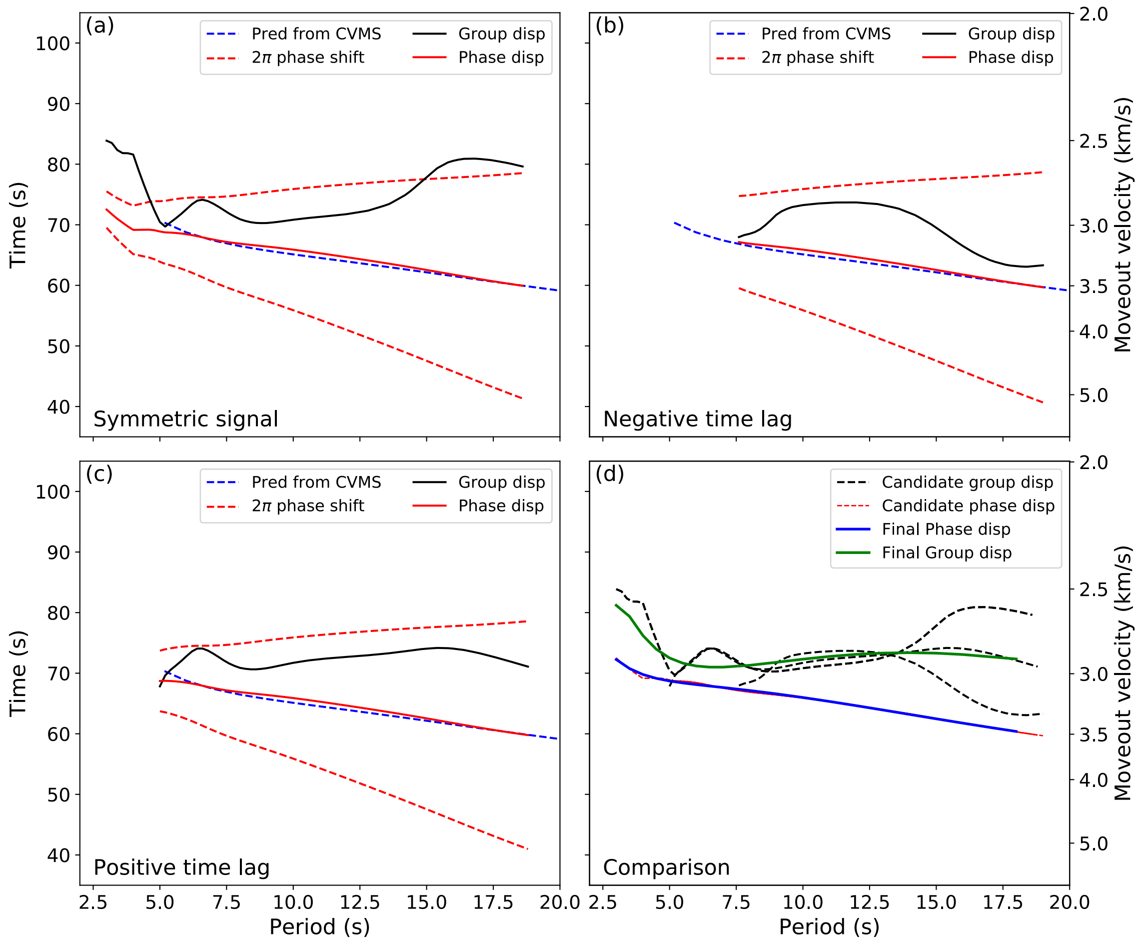

(a)
Pred from CVMS
Group disp
2π phase shift
Phase disp
Symmetric signal
(b)
Negative time lag
(c)
Positive time lag
(d)
Candidate group disp
Candidate phase disp
Final Phase disp
Final Group disp
Comparison
Time (s)
Moveout velocity (km/s)
Period (s)

Figure 6

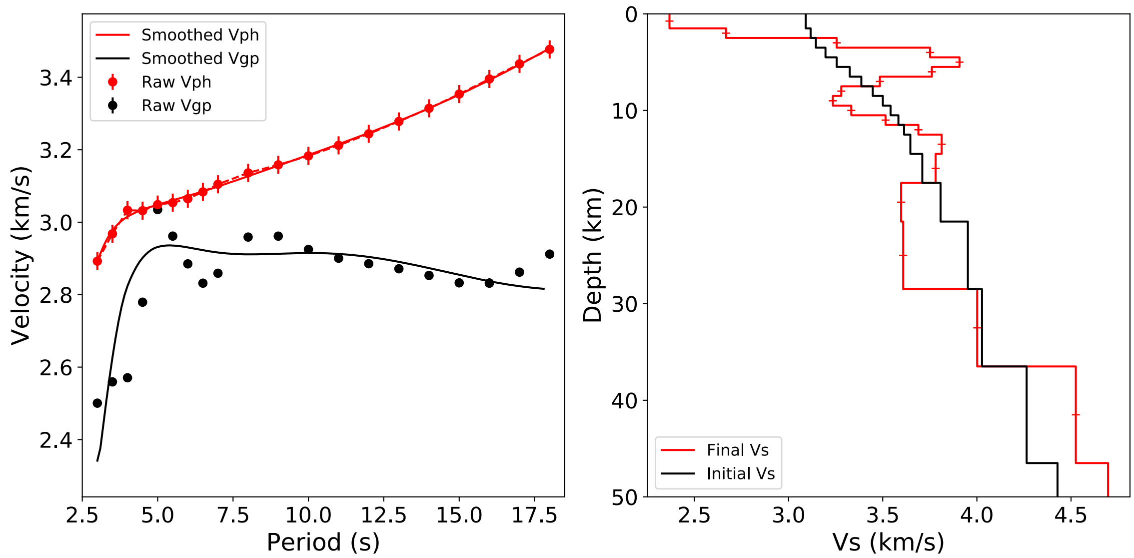
Smoothed Vph
Smoothed Vgp
Raw Vph
Raw Vgp
Velocity (km/s)
Period (s)
Final Vs
Initial Vs
Depth (km)
Vs (km/s)

Figure 7

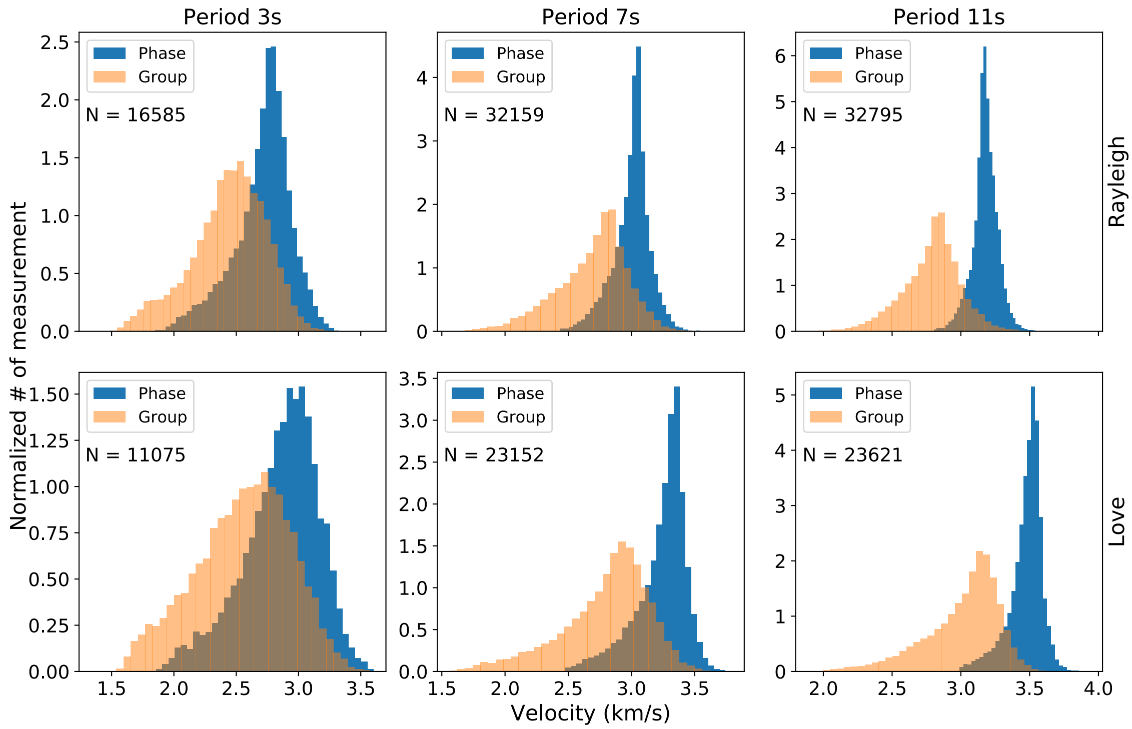

Period 3s
Period 7s
Period 11s
Phase
Group
N = 16585
N = 32159
N = 32795
N = 11075
N = 23152
N = 23621
Rayleigh
Love
Normalized # of measurement
Velocity (km/s)

Figure 8

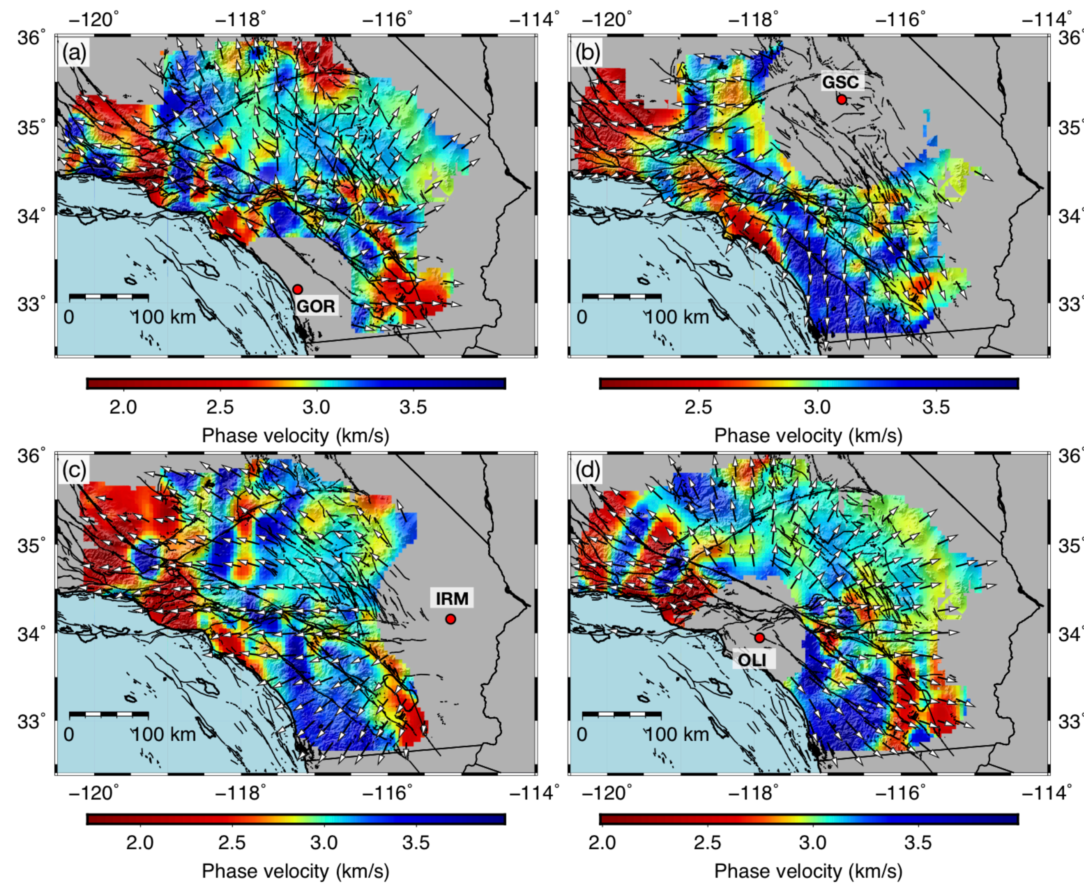

Figure 9

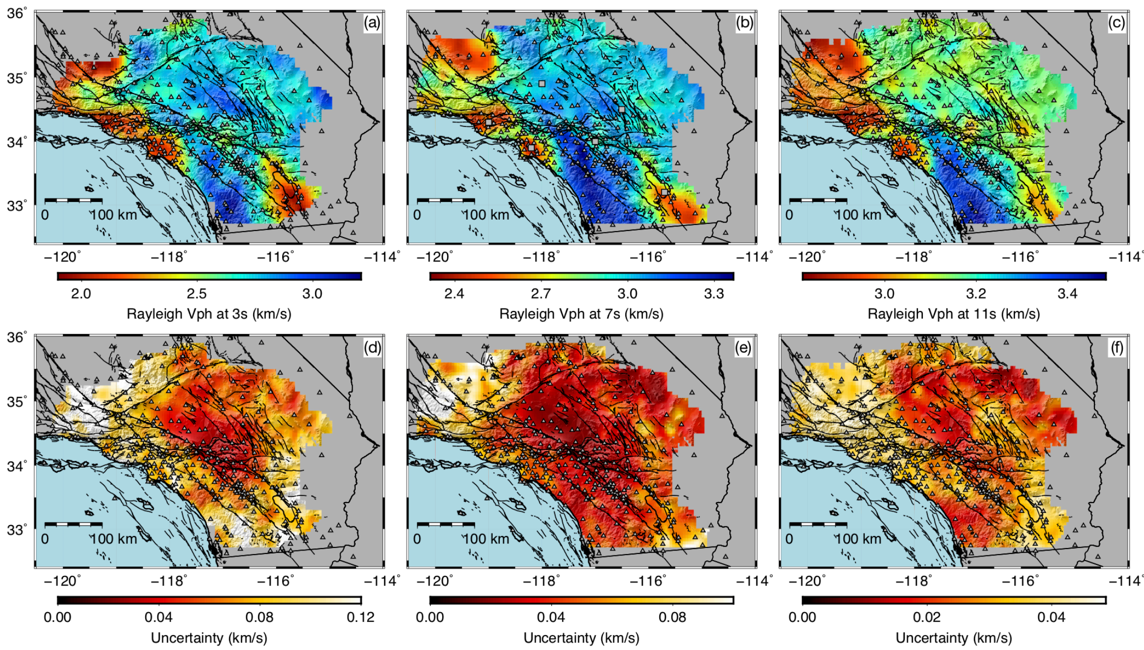

36°
35°
34°
33°
(a)
(b)
(c)
(d)
(e)
(f)
0
100 km
−120°
−118°
−116°
−114°
2.0
2.5
3.0
Rayleigh Vph at 3s (km/s)
2.4
2.7
3.0
3.3
Rayleigh Vph at 7s (km/s)
3.0
3.2
3.4
Rayleigh Vph at 11s (km/s)
0.00
0.04
0.08
0.12
Uncertainty (km/s)
0.00
0.04
0.08
Uncertainty (km/s)
0.00
0.02
0.04
Uncertainty (km/s)

Figure 10

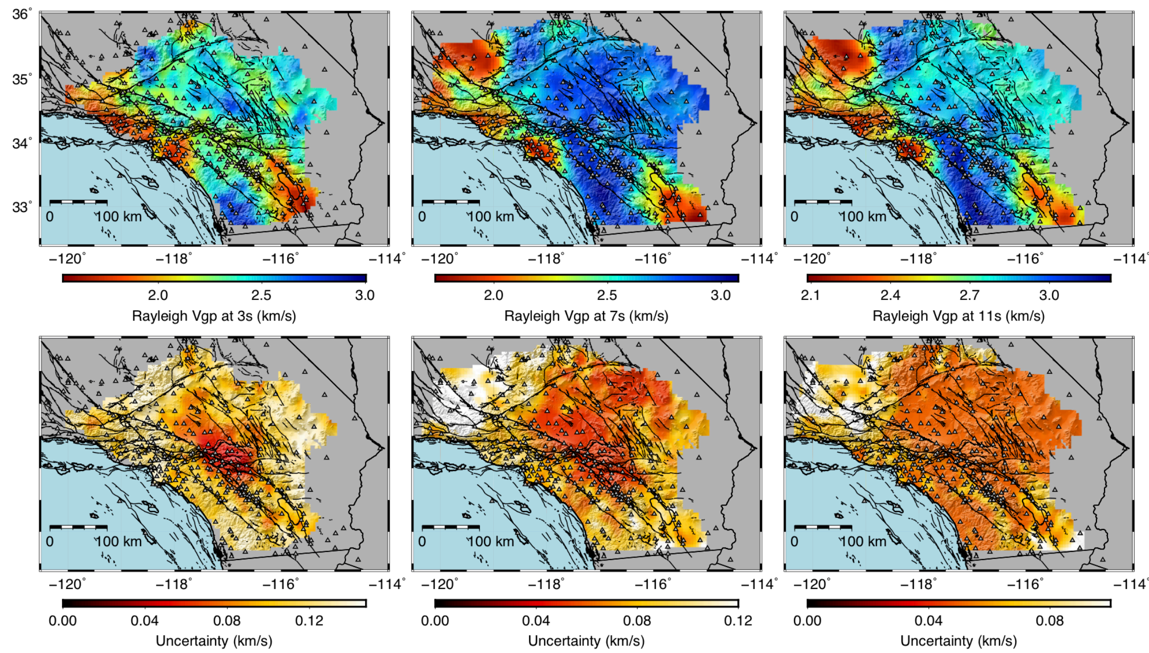

36°
35°
34°
33°
0
100 km
−120°
−118°
−116°
−114°
2.0
2.5
3.0
Rayleigh Vgp at 3s (km/s)
Rayleigh Vgp at 7s (km/s)
2.1
2.4
2.7
3.0
Rayleigh Vgp at 11s (km/s)
0.00
0.04
0.08
0.12
Uncertainty (km/s)

Figure 11

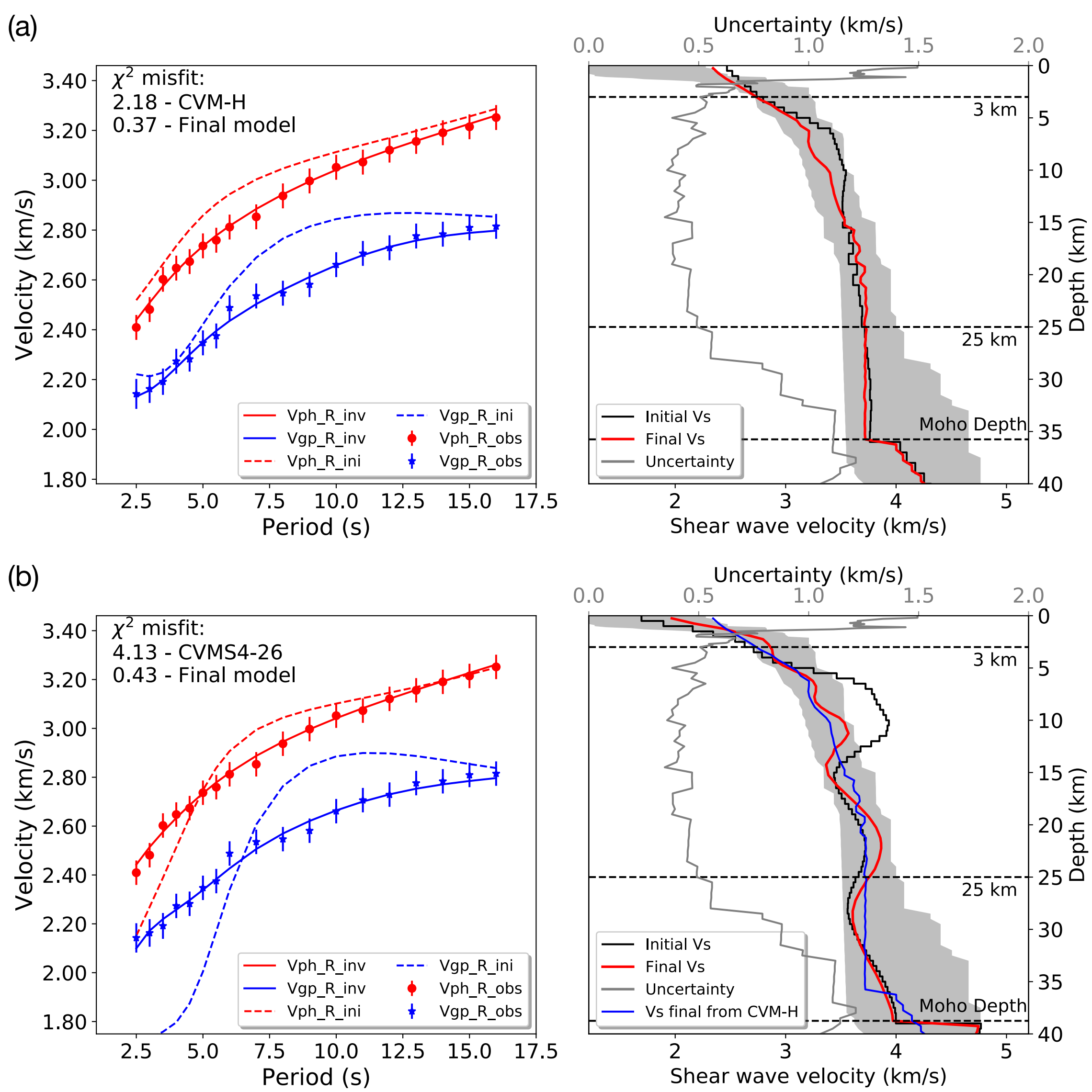

(a)
χ^2 misfit:
2.18 - CVM-H
0.37 - Final model
Velocity (km/s)
Period (s)
Vph_R_inv
Vgp_R_inv
Vph_R_ini
Vgp_R_ini
Vph_R_obs
Vgp_R_obs
Uncertainty (km/s)
3 km
25 km
Moho Depth
Depth (km)
Initial Vs
Final Vs
Uncertainty
Shear wave velocity (km/s)
(b)
χ^2 misfit:
4.13 - CVMS4-26
0.43 - Final model
Vs final from CVM-H

Figure 12

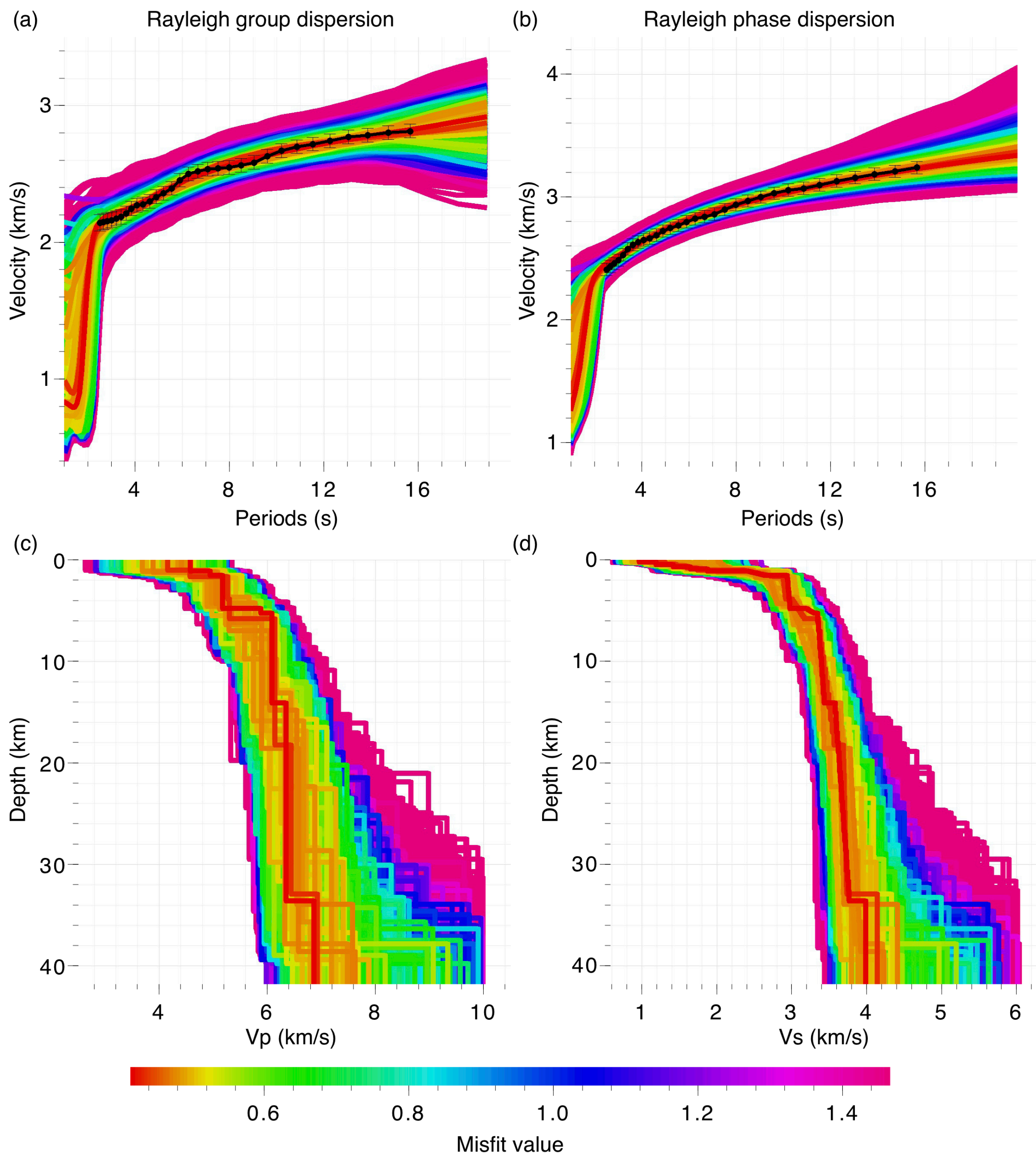
(a)
Rayleigh group dispersion
Velocity (km/s)
Periods (s)
(b)
Rayleigh phase dispersion
Velocity (km/s)
Periods (s)
(c)
Depth (km)
Vp (km/s)
(d)
Depth (km)
Vs (km/s)
Misfit value

Figure 13

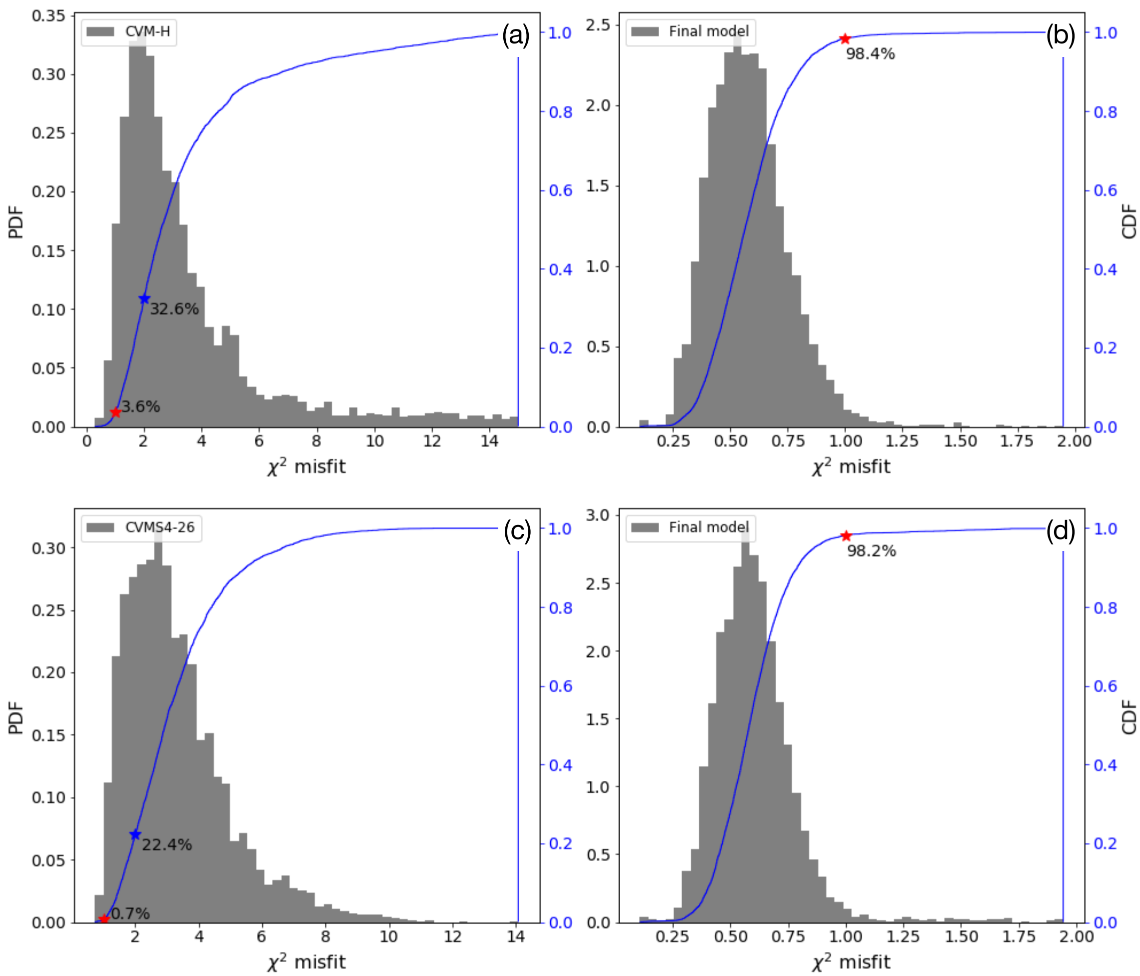

CVM-H
(a)
32.6%
3.6%
Final model
(b)
98.4%
CVMS4-26
(c)
22.4%
0.7%
Final model
(d)
98.2%
PDF
CDF
χ^2 misfit

Figure 14

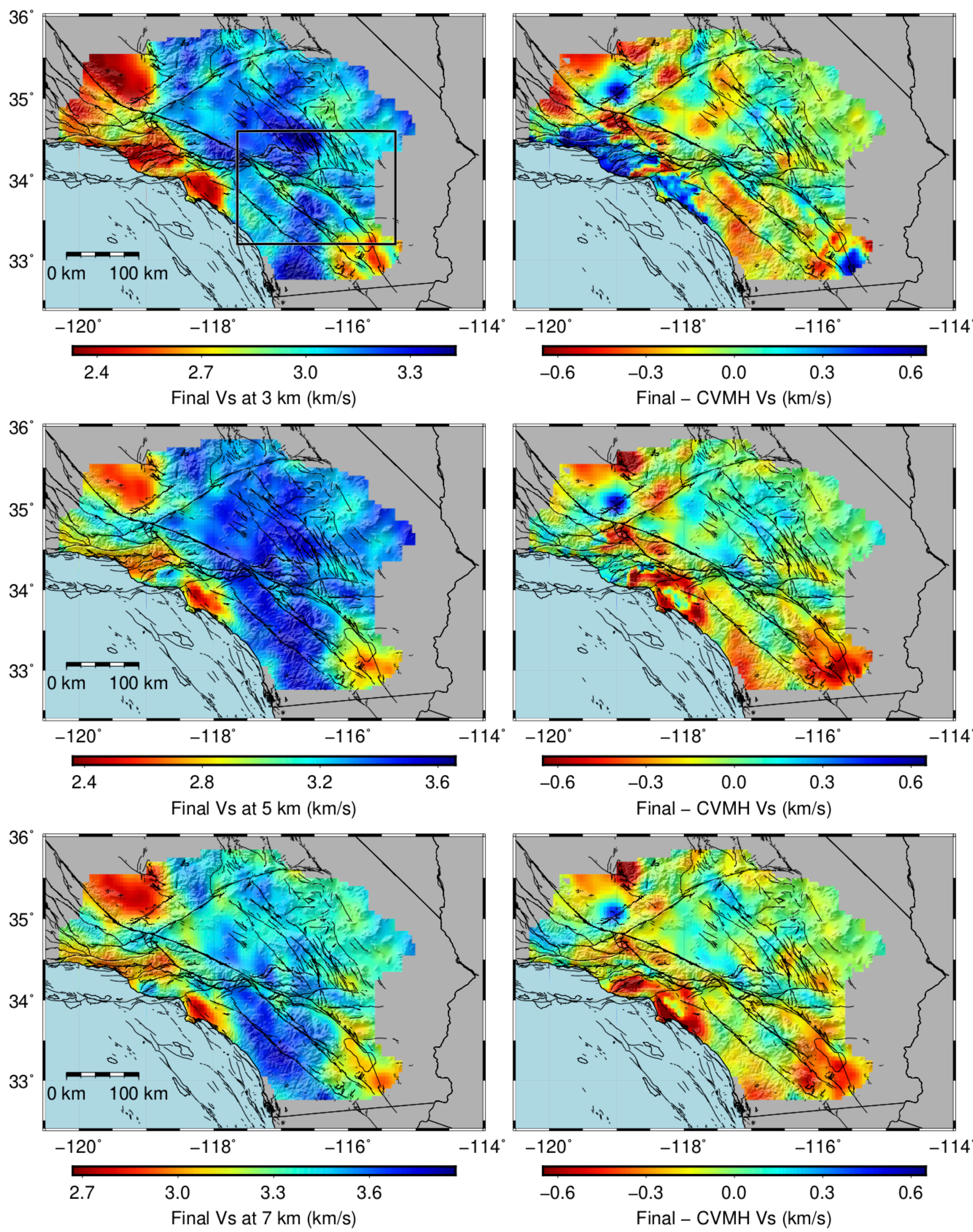
36˚
35˚
34˚
33˚
0 km
100 km
−120˚
−118˚
−116˚
−114˚
2.4
2.7
3.0
3.3
Final Vs at 3 km (km/s)
−0.6
−0.3
0.0
0.3
0.6
Final − CVMH Vs (km/s)
2.4
2.8
3.2
3.6
Final Vs at 5 km (km/s)
Final − CVMH Vs (km/s)
2.7
3.0
3.3
3.6
Final Vs at 7 km (km/s)
Final − CVMH Vs (km/s)

Figure 15

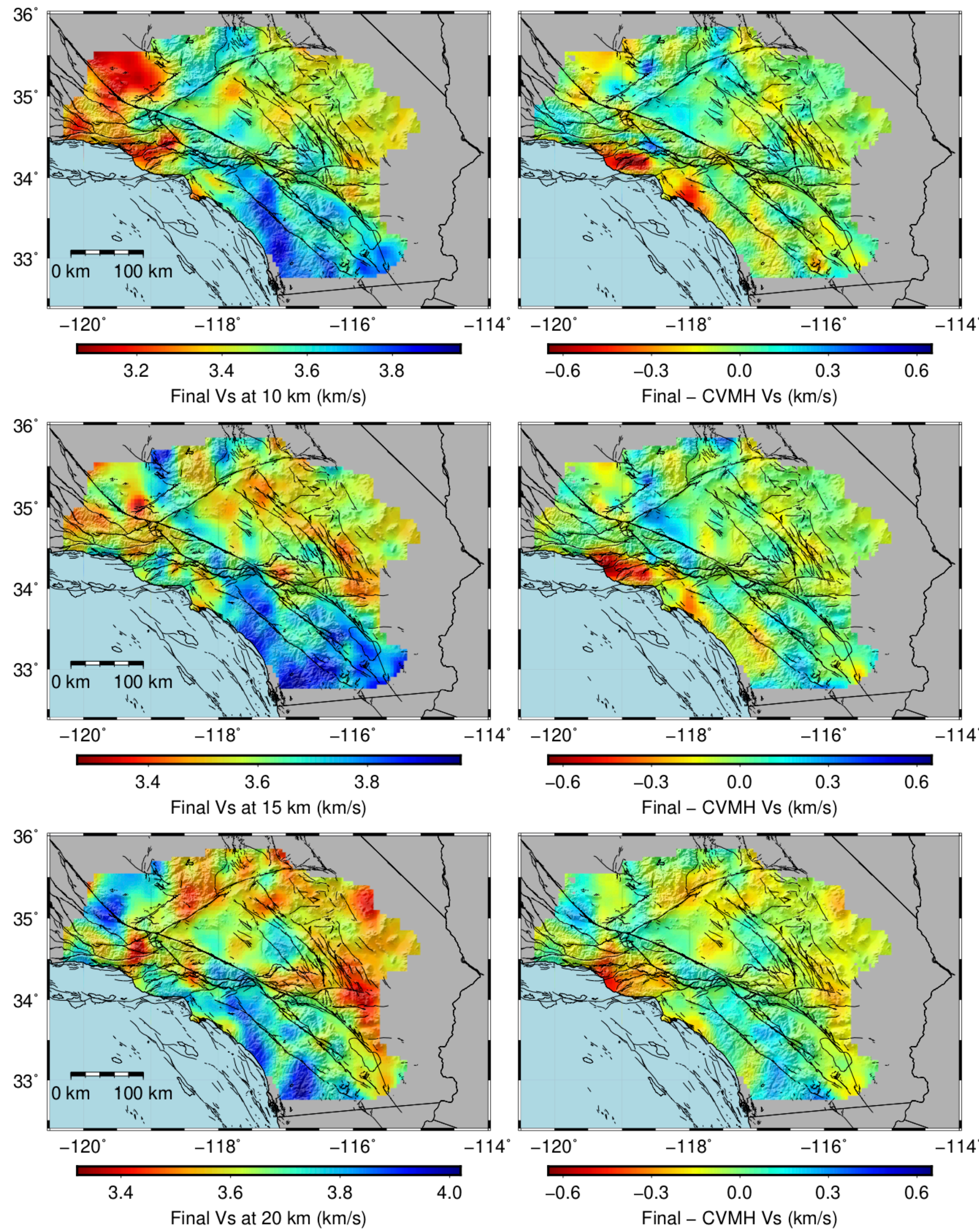
36˚
35˚
34˚
33˚
0 km
100 km
−120˚
−118˚
−116˚
−114˚
3.2
3.4
3.6
3.8
Final Vs at 10 km (km/s)
−0.6
−0.3
0.0
0.3
0.6
Final − CVMH Vs (km/s)
3.4
3.6
3.8
Final Vs at 15 km (km/s)
Final − CVMH Vs (km/s)
3.4
3.6
3.8
4.0
Final Vs at 20 km (km/s)
Final − CVMH Vs (km/s)

Figure 16

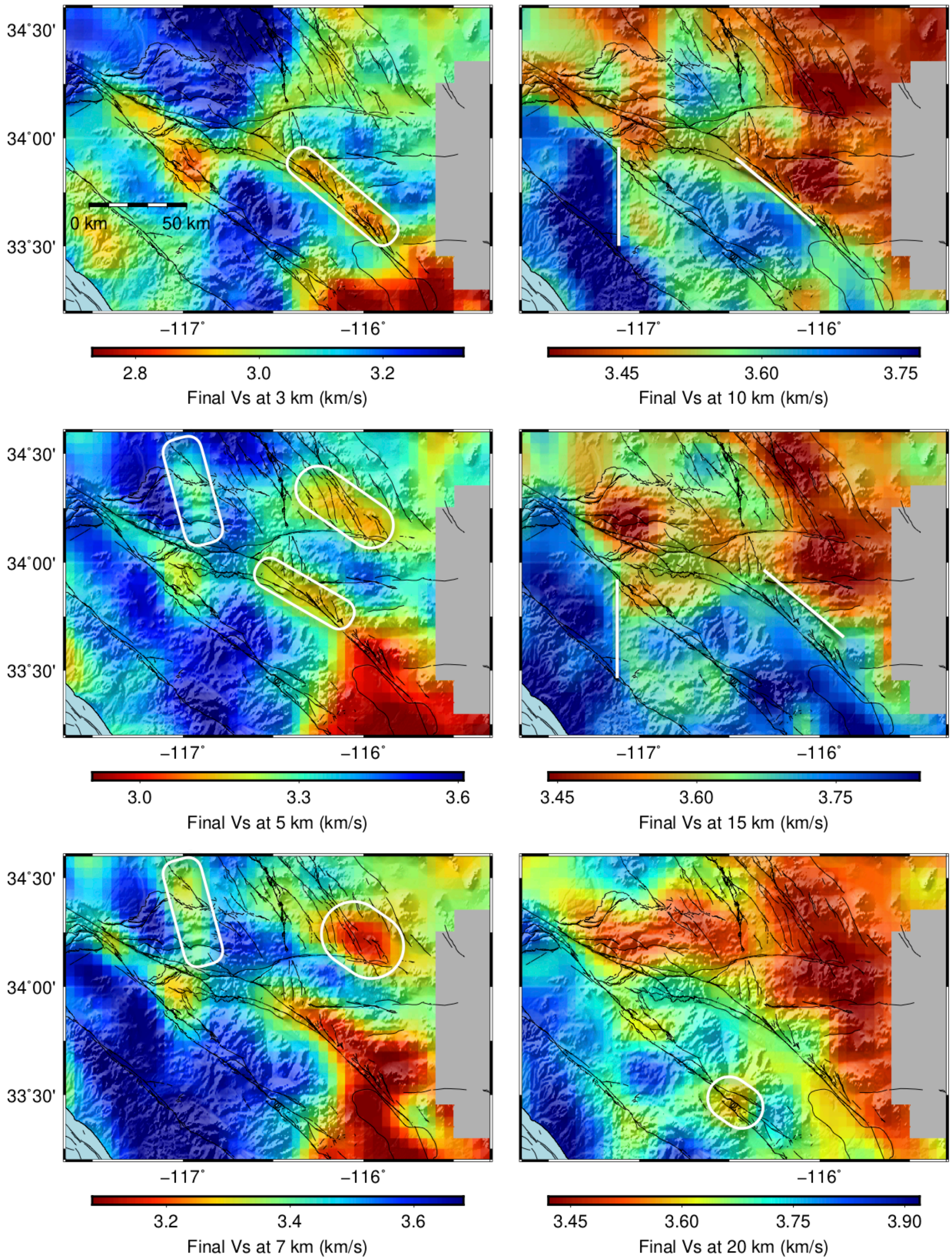
34°30'
34°00'
33°30'
0 km
50 km
–117°
–116°
2.8
3.0
3.2
Final Vs at 3 km (km/s)
3.45
3.60
3.75
Final Vs at 10 km (km/s)
3.0
3.3
3.6
Final Vs at 5 km (km/s)
3.45
3.60
3.75
Final Vs at 15 km (km/s)
3.2
3.4
3.6
Final Vs at 7 km (km/s)
3.45
3.60
3.75
3.90
Final Vs at 20 km (km/s)

Figure 17

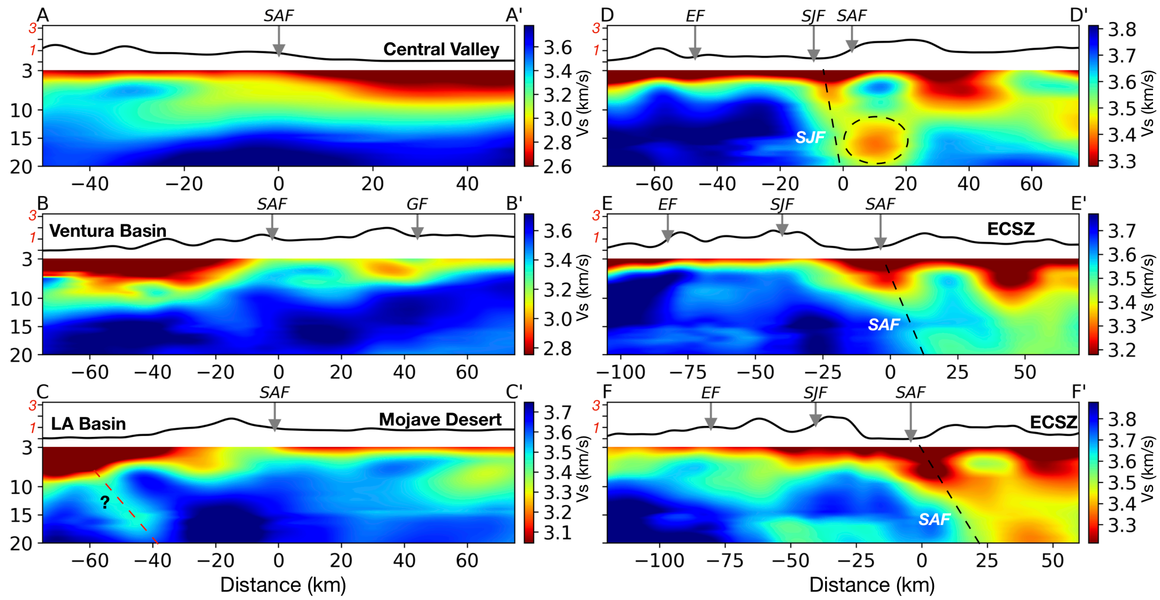

A
A'
SAF
Central Valley
Vs (km/s)
D
D'
EF
SJF
SAF
SJF
Vs (km/s)
B
B'
SAF
GF
Ventura Basin
Vs (km/s)
E
E'
EF
SJF
SAF
ECSZ
SAF
Vs (km/s)
C
C'
SAF
LA Basin
Mojave Desert
?
Vs (km/s)
Distance (km)
F
F'
EF
SJF
SAF
ECSZ
SAF
Vs (km/s)
Distance (km)

Figure 18